Climate Dynamics
https://doi.org/10.1007/s00382-020-05376-2

El Niño phase-dependent high-frequency variability in Western Equatorial Pacific

Ming Sun[1] · **Tim Li**[1,2] · **Lin Chen**[1,3,4]

Received: 26 October 2019 / Accepted: 11 July 2020

Abstract
The intensities of high-frequency (HF) variability with period less than 90 days at different phases of El Niño events were investigated through observational data analysis. A large asymmetry in the HF variability intensity between the developing phase and decaying phase (i.e., pre-peak stage versus post-peak stage) of eastern Pacific (EP) El Niño is revealed, while the amplitude and spatial pattern of the sea surface temperature anomaly during these two stages are almost same. The diagnosis shows that the asymmetry is significant not only on intraseasonal time scale (20–90 days) but also on synoptic time scale (less than 20 days). The anatomy analysis further unveils that the asymmetric synoptic variability between the two episodes arises from the asymmetric intensities of the equatorial Rossby and mixed Rossby gravity (MRG) waves. We suggest that the stronger vertical easterly wind shear in the pre-peak stage than that in the post-peak stage plays a vital role in causing the stronger synoptic equatorial Rossby and MRG waves in the pre-peak stage. Meanwhile, the drier atmosphere and more descending motion in the post-peak stage contribute to the weakened intraseasonal and synoptic variabilities in that stage. The aforementioned weakened easterly wind shear, drier atmosphere and more descending motion in the post-peak stage can be traced back to the occurrence of the anomalous anticyclone circulation over the western North Pacific since the decaying phase of El Niño. The essential role of large-scale environmental conditions in modulating the HF variability during the two episodes is further confirmed by modeling experiments.

Keywords El Niño · Asymmetric high-frequency variability · Vertical wind shear · Western North Pacific anticyclone

✉ Ming Sun
18252087820@163.com

Tim Li
timli@hawaii.edu

[1] Key Laboratory of Meteorological Disaster, Ministry of Education (KLME)/Joint International Research Laboratory of Climate and Environmental Change (ILCEC)/ Collaborative Innovation Center on Forecast and Evaluation of Meteorological Disasters (CIC-FEMD), Nanjing University of Information Science and Technology, Nanjing, China

[2] International Pacific Research Center and Department of Atmospheric Sciences, School of Ocean and Earth Science and Technology, University of Hawaii at Manoa, Honolulu, HI 96822, USA

[3] State Key Laboratory of Numerical Modeling for Atmospheric Sciences and Geophysical Fluid Dynamics (LASG), Institute of Atmospheric Physics, Chinese Academy of Sciences, Beijing 100029, China

[4] State Key Laboratory of Satellite Ocean Environment Dynamics, Second Institute of Oceanography, Hangzhou, China

1 Introduction

The El Niño-southern oscillation (ENSO) is one of the primary and fundamental low-frequency modes on earth, with a period of 2–8 years in interannual scales. ENSO, as a strong coupled system between atmosphere and ocean (e.g., Lau 1981; Philander et al. 1984; Anderson et al. 1985; Cane and Zebiak 1985; Neelin 1991; Guilyardi et al. 2009; Su et al. 2018; Chen et al. 2019a, b, Park et al. 2019), alternates between warm (El Niño) and cold (La Nina) sea surface temperature (SST) condition. It has enormous influences on natural system in large scale, not only confined in ocean system but also other processes in atmosphere system. For example, in ocean system, equatorial wind anomalies associated with ENSO's anomalous SST cause oceanic Kelvin waves along the west coast of the Americas (Clarke et al. 1994). In atmosphere system, the anomalous vorticity at upper level due to ENSO drives the atmospheric Rossby waves in large scales propagate to extra tropic (Trenberth

Published online: 06 August 2020

et al. 1998), associated with the generation of Pacific-North-American pattern (Horel et al. 1981).

Recent studies have gradually recognized that in relative to the interannual variability of ENSO-related signals, the high-frequency (HF, with periods less than 90 days) variability of surface zonal wind in the western-central equatorial Pacific play a vital role in triggering and maintaining the ENSO events (Sui and Lau 1992; Sui et al. 1997, 1999; Kessler and Kleeman 2000; Boulanger et al. 2004; Hong and Li 2009; Hong et al. 2010; Rong et al. 2011; Li and Ren 2012; Chiodi et al. 2014; Chen et al. 2016a, b, 2017; Wang et al. 2015, 2018, 2019). The HF variability of surface zonal wind generally contains two major components: the synoptic time scale wind and the intraseasonal time scale wind. The former is usually composed by the so-called westerly wind bursts (hereafter WWBs) or westerly wind events (WWE). It is a short-lived anomalous westerly wind with large magnitude over tropical Pacific (Harrison and Vecchi 1997; Seiki and Takayabu 2007a, b), which could impact the onset and development of El Niño. On one hand, WWBs cause eastward downwelling Kelvin wave by deepening equatorial thermocline, thus leading to warming SST signals (McPhaden et al. 1988; McPhaden 1999); on the other hand, they generate strong eastward surface currents which make the warm pool extend eastward (Picaut et al. 1997). WWBs exert great influence on El Niño irregularity and diversity by the two ways (Lengaigne et al. 2004; Hu et al. 2014; Lian et al. 2014; Fedorov et al. 2015; Chen et al. 2015, 2016a, 2017; Hayashi and Watanabe 2017). For example, Chen et al. (2015) conducted the numerical experiments superposed the WWB-like perturbation into an ocean–atmosphere coupled model with a regular oscillation of SST anomalies in central-eastern Pacific, and found that it directly leads to the increase of both strong warm events in eastern Pacific and weak warm events near dateline. The later canonical high-frequency wind disturbance is usually related to MJO, which is the dominant component of intraseasonal variability in tropical atmosphere with planetary zonal scale (Madden and Julian 1971, 1972). It has eastward zonally oriented convective disturbance and the major circulation anomalies are in zonal wind. More and more studies have documented that MJO shows considerable impacts on ENSO variability. Like WWBs, MJO could also excite downwelling Kelvin wave (Kessler et al. 1995; Hendon et al. 1998), and thus could induce and modulate ENSO through two processes mentioned above (Kessler and Kleeman 2000; Zhang and Gottschalck 2002). Although these previous studies (e.g., Kessler and Kleeman 2000; Zhang and Gottschalck 2002; Puy et al. 2016) suggested that both WWB and MJO can set up favorable conditions for the development of the El Niño-related sea surface temperature anomaly (SSTA); Chiodi et al. (2014) argued that it is WWB, rather than MJO, that plays the essential role in impacting El Niño-related SSTA. These debates were comprehensively studied by Feng and Lian (2018), who pointed out that the difference in the relationship between WWBs and MJO shown in previous works is primarily due to the ambiguous definition of the two phenomena, especially of the WWBs. When WWBs and MJO are defined in a clear and reasonable way, they found that although MJO favors the genesis of WWBs, it is not the main driver of WWBs. They also suggested that only the WWB plays a vital role in influencing El Niño-related SSTA, whereas the MJO events that occurred without WWB events play a minor role in influencing El Niño-related SSTA.

Despite of the aforementioned debate, the origin and genesis of WWBs received more and more attention recently (Chiodi et al. 2014; Puy et al. 2016; Chen et al. 2016c; Feng and Lian 2018; Lian et al. 2018a, b; Fu and Tziperman 2019). WWBs were regarded as the stochastic noise in the atmosphere which is independent of ENSO variability for a long time, partly due to the large gap between time scales of WWBs and ENSO. During the past two decades, people gradually recognized that the "stochastic noise" of the HF surface wind disturbance (e.g., the WWB) is state-dependent and can be largely modulated by interannual variability of SST through conducting the observational analysis and numerical experiments (Yu et al. 2003; Eisenman et al. 2005; Kug et al. 2009b; Gushchina and Dewitte 2012). For instance, the observation evidences show that the WWBs tend to occur more frequently when warm pool extends (Yu et al. 2003), and the frequency of WWBs has a close relationship with the variation of SSTA in Niño3-region (Seiki and Takayabu 2007a, b). Kug et al. (2008) even found that WWBs tend to be more active during warm ENSO events than cold events. Using a hybrid coupled model, Gebbie et al. (2007) found that the parameterized locations of WWBs vary with the edge of warm pool, which further leads to coupled feedbacks between SST and WWBs. Likewise, the intraseasonal disturbances associated with MJO are also influenced by interannual variation of SST in many ways. Some theories suggested that SST is a critical factor affecting the propagation speed and period of MJO activities (Lau and Shen 1988; Davey 1989). During ENSO warm events, the warm pool extends eastward, so does the MJO activities (Anyamba and Weare 1995; Hendon et al. 1999). Some studies further found that different ENSO phases-related SST anomalies have different effects on MJO activities, e.g., the intensity of MJO tends to be more active before the peak of ENSO warm events and weaker after the peak of cold events (Zhang and Gottschalck 2002; Lau 2005).

From above all, both WWBs and MJO are affected by large-scale SST field a lot. However, few studies have paid attention to the contrasting modulation effects between the development stage and decaying stage of El Niño event. It is not clear whether or not the SST during different life stages

of El Niño events would play different roles in modulating the HF variability of surface wind, and if the answer is yes, what is the mechanism responsible for the distinctive effects? Motivated by these questions, in the following we will firstly show that the HF wind variabilities are distinctively different between the two stages, even the SST anomalies are quite similar with each other. Then we would investigate the potential factors for the contrasting performance and conduct numerical experiments to test our hypotheses.

The remainder of this paper is organized as below. In Sect. 2, the data and model we used in this study are briefly described. In Sects. 3 and 4, the variations of high-frequency variabilities are shown. The potential factors impacting on intensity's difference are analyzed in Sect. 5. And in Sect. 6, the favorable factors for the growth of high-frequency variabilities are examined. A summary and discussion are given in the final section.

2 Data and methodology

The observation datasets and reanalyses used in this study include: (1) the monthly SST data with 2°×2° resolution from global sea surface temperature is obtained from National Oceanic and Atmospheric Administration (NOAA) extended reconstructed sea surface temperature (ERSST) v3b (Smith et al. 2008); (2) the daily advanced very high-resolution radiometer (AVHRR) Outgoing Longwave Radiation (OLR) data from the NOAA polar orbiting satellite (Liebmann and Smith 1996) with a 2.5° grid; (3) the daily wind data with a 1.5° horizontal resolution covering the period of 1979–2016

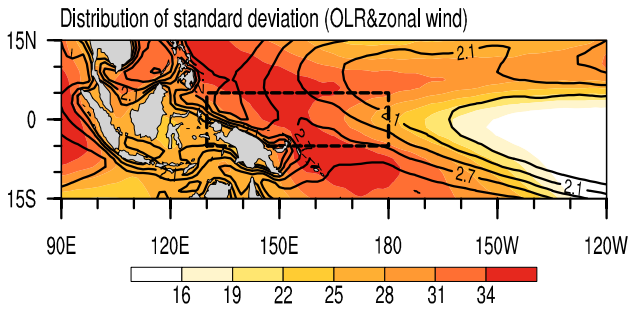

Fig. 1 Distribution of standard deviation of high-frequency (0–90 days) OLR (W m^{-2}, shaded) and zonal wind (m s^{-1}, contour). The black dash lines mark the region in western equatorial Pacific researched

derived from the global atmospheric Interim European Centre for Medium-Range Weather Forecast (ECMWF) Re-Analysis (ERA-Interim; Dee et al. 2011).

Most of intraseasonal and synoptic disturbances assemble in western equatorial Pacific. Figure 1 shows the climatological distribution of standard deviation of OLR and zonal wind at 1000 hPa over western equatorial Pacific. The maximum of OLR and zonal wind's deviation both assemble in the region enclosed by black lines. To the east of date line, the standard deviation of OLR and zonal wind quickly diminish, which is consistent with the results reported by previous studies. In this study, we will mainly concentrate on the high-frequency variability of surface zonal wind in the western equatorial Pacific region 5° S–5° N, 130° E–180°; hereafter WEP). Note that same results can be found if the zonal wind at 850 hPa is utilized to represent surface zonal wind variability.

To investigate the role of El Niño in modulating the atmospheric HF variability, we selected the El Niño events during 1979–2016 to conduct the composite analysis, based on the three-months running mean Nino3.4 index from 1979 to 2016. As we know, in the recent decades, the warming center of El Niño events tends to occur in central Pacific more frequently, compared to the canonical warming position that located in the eastern Pacific. On basis of spatial distribution of SST warming center, various terminations were employed for this new type of El Niño events, including the dateline El Niño, central Pacific El Niño, El Niño modoki, and warm pool El Niño (Larkin and Harrison 2005; Ashok et al. 2007; Kao and Yu 2009; Kug et al. 2009a). Hereafter, we used the termination of central Pacific (CP) El Niño instead of the aforementioned several terminations. As different warming patterns have different influences on the atmosphere and ocean system (Feng et al. 2016, 2017; Weng et al. 2007; Chen et al. 2018), the impacts of different types of El Niño on the high-frequency variability in the atmosphere will be discussed in separate. According to the classification proposed by Kao and Yu (2009) and Yu and Kim (2013), Table 1 lists the types of El Niños events from 1979 to 2016, including three conventional eastern Pacific (EP) El Niño and other non-EP types of El Niños (CP type and Mixed type events). It is worth mentioning that the special prolonged El Niño event during 1986–1988, due to its successive life period and the unique evolution of SSTA, was not discussed in this study. It is interesting to note that both the EP and other non-EP types of El Niños have the warmest SSTA signals in or nearby December, however, the performance of the atmospheric high-frequency variability are distinctive between the

Table 1 Identification of El Niño events since the 1980s, based on the classification method proposed by Kao and Yu (2009) and Yu and Kim (2013)

EP El Niños	1982–1983, 1997–1998, 2015–2016
Other El Niños	1987–1988, 1991–1992, 1994–1995, 2002–2003, 2004–2005, 2009–2010 (CP type); 1986–1987, 2006–2007 (mixed type)

stage prior to the peak phase (pre-peak phase) and the stage after the peak phase (post-peak phase), which will be investigated in details in this study.

In this study, we employed a linear anomaly atmospheric general circulation model (AGCM) to examine the influence of background conditions on the intensity of high-frequency disturbances. This model derived from GFDL global spectrum dry AGCM (Held and Suarez 1994) and was developed by Tim Li in other researches (Wang et al. 2003; Jiang and Li 2005; Li 2006). In this global spectrum model, five sigma ($\sigma = p/p_s$) levels with an interval of 0.2 are used as its vertical coordinate (a top level at $\sigma = 0$, and a bottom level at $\sigma = 1$). The basic equations in the model include momentum, temperature, and logarithm of surface pressure equations together with a diagnostic equation for the vertical velocity. The horizontal resolution in this study is T42. The same biharmonic diffusion is applied to momentum and temperature equations with a diffusion rate of 0.1 day^{-1}. In the experiments, the AGCM is run on an "aquaplanet" earth, in which the topography is ignored, and the SST distribution is distinguishable in the meridional direction but uniform in the zonal direction. To mimic the planetary boundary layer, Rayleigh friction is applied to the momentum equations, with the damping rate of 1 day^{-1} at the lowest model level, $\sigma = 0.9$, linearly decaying to 0.1 day^{-1} at the level of $\sigma = 0.7$. Newtonian cooling with an *e*-folding time scale of 10 days is applied to the temperature equations at all model levels. To focus on tropical perturbations, a strong damping rate of 1 day^{-1} is applied in the perturbation momentum and temperature equations over regions with latitude beyond 40° S and 40° N.

3 Variation of high-frequency's intensity during typical El Niño

Following the strategy designed by Hendon et al. (2007), we employed a HF activity index to quantify the intensity of HF variability. Firstly, we calculated the time series of daily zonal wind anomaly at 1000 hPa (U′) at each grid point, and then obtained the high-frequency component (less than 90 days) of zonal wind anomaly ($U'|_{<90d}$) with the Lanczos high-pass filter (Duchon 1979). Then the standard deviation of $U'|_{<90d}$ is computed over a certain 90 day running period to represent the HF variability in the particular period, and the value averaged over WEP can be defined as the index describing the intensity of HF activity over WEP. Figure 2a shows the composite result of the evolution of the high-frequency index (HFI) of $U'|_{<90d}$ averaged over WEP (black solid line) and the Niño3.4 index (red solid line) during the El Niño events. The Niño3.4 index appears to be symmetric with respect to the peak phase of El Niño events—November(0)December(0)January(+1) [i.e., ND[0]J(+1)], that

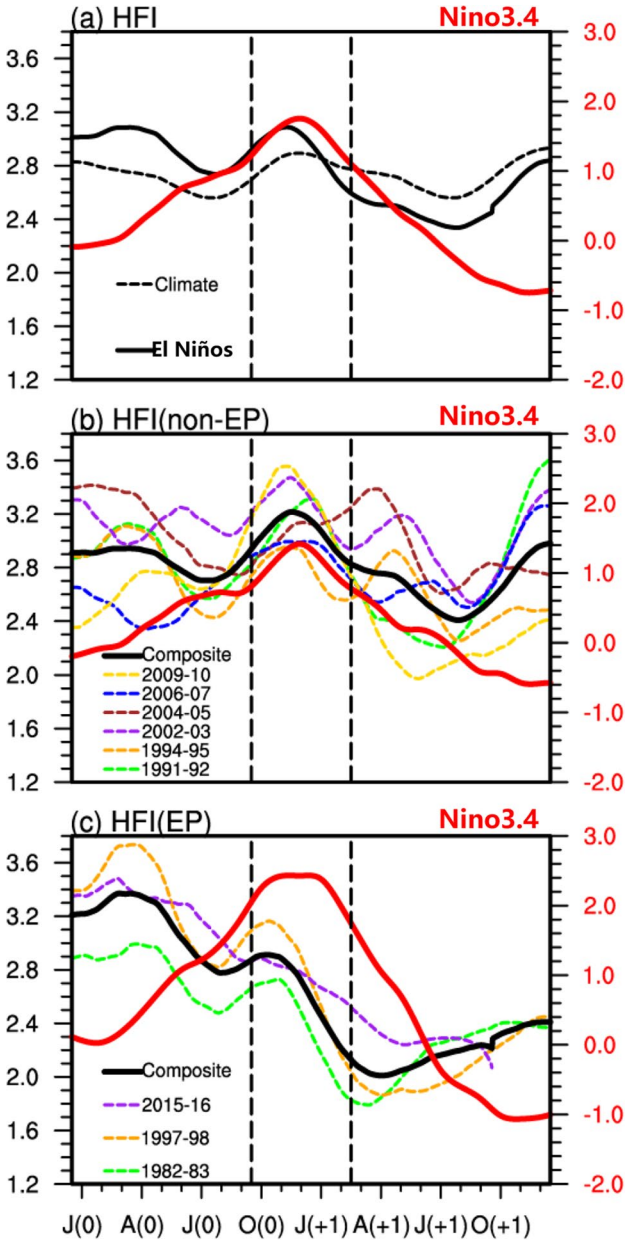

Fig. 2 Variations of HFI calculated by high-frequency zonal wind at 1000 hPa in western equatorial Pacific for **a** the composite of HFI during El Niños (black solid) and climatological state (black dash). The corresponding composite results from **b** the non-EP El Niño group and **c** EP El Niño group. The scale interval for HFI is shown in left-hand Y-axis (unit: m s^{-1}). The red line (unit: K; scale interval is shown in right-hand Y-axis) denotes the variation of Niño3.4 index in each group

is, the magnitude of SSTA during the pre-peak phase and post-peak phase is comparable. However, the evolution of the intensity of HF wind disturbances shows a significant asymmetry feature between the pre-peak phase stage and the post-peak phase stage. In particular, the SSTA averaged over Niño3.4 region is approximately one degree during

both September–October (0) of the developing stage (hereafter SO(0)) or February–March (+1) of the decay stage (hereafter FM(+1)), while the HF zonal wind variability is more active during SO(0) than that during FM(+1), which is significant at 90% confidence level. However, from the perspective of long-term climatological mean (see the black dashed line), the HF variability of zonal wind disturbance in WEP is weaker during the El Niño developing stage than that during the El Niño decay stage. The distinction between the composite El Niño results and the climatological mean indicates that the interannual SST anomaly (SSTA) plays a critical role in rectifying the HF variability of surface zonal wind. Then we further check the performance of the HF variability during the two types of El Niño events in separate. During the evolution of other types of El Niños (Fig. 2b), both the Niño3.4 indices and the intensity of high-frequency's disturbances are comparable between SO(0) and FM(+1). In contrast, during the evolution of EP El Niños (Fig. 2c), the Niño3.4 index is comparable during the two stages before and after the peak phase, while the intensity of the HF disturbances is pronouncedly stronger during the pre-peak stage than that during the post-peak stage. This raises a question that what causes the difference in the HF surface wind disturbances between the developing stage and the decay stage of EP El Niño events.

To refine the origin of the difference in HF surface zonal wind variability between SO(0) and FM(+1) of EP El Niño events, we further decomposed the HF surface zonal wind variability into two different timescale components. Using the Lanczos bandpass filter (Duchon 1979), we also obtained the strength of the intraseasonal surface zonal wind variability with period between 20 and 90 days (see the middle bars in Fig. 3) and synoptic variability with periods less than 20 days (right bars in Fig. 3). As shown in Fig. 3, the differences in both the intraseasonal (20–90 days) and synoptic (<20 days) timescales contribute to the difference in HF surface wind variability between SO(0) and FM(+1). Here the whiskers in Fig. 3 presented the spread across the cases (which is measured by a standard deviation among the cases). As clearly indicated by the whiskers, the strength of both the intraseasonal zonal wind variability and synoptic zonal wind variability is significantly stronger in SO (0) than that in FM (+1). From the perspective of the difference between SO(0) and FM(+1) (see the grey bars), the contrasting HFI between pre-peak stage and post-peak stage arises from the difference in both intraseasonal component and synoptic component. Note that the activities in intraseasonal and synoptic scales are actually complicated, and the classification we adopted here is a rough method just considering time periods. In the following analyses, we will further present more details about characteristics on structures of intraseasonal and synoptic disturbances in these two stages, i.e., SO(0) and FM(+1).

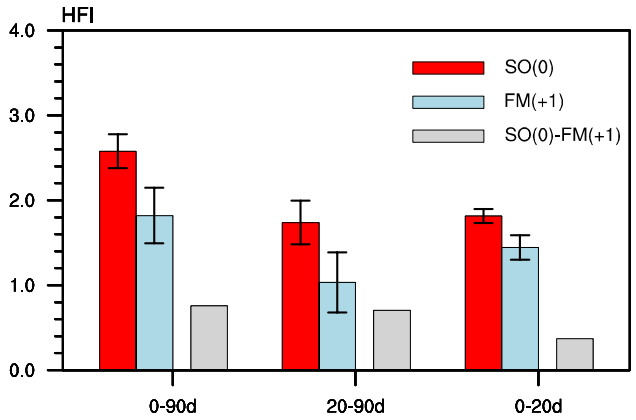

Fig. 3 HFI of high-frequency zonal wind at 1000 hPa in SO(0) (red bars) and in FM(+1) (blue bars) during EP El Niño, for three timescales (high-frequency, 0–90 days; intraseasonal, 20–90 days; synoptic, 0–20 days). The whiskers indicate the standard deviations among cases

According to some previous researches (Yu et al. 2003; Batstone and Hendon 2005), SST is one of the factors that influence the intensity of high-frequency disturbances. Then it is worth noting that during EP El Niños, the Niño3.4 indices in SO (0) and FM (+1) are approximate, associated with similar background SST in these two periods (shown in Fig. 9c, d). However, apparent decrease of high-frequency intensity only can be seen in EP El Niños. It indicates that something else influences the alternation of high-frequency zonal wind in western equatorial Pacific apart from the SST's effect. Therefore, the possible factors which get rise to the intensity's differences of high-frequency disturbances between SO (0) and FM (+1) during EP El Niños, are discussed in Sect. 6.

4 Spatial–temporal features of the HF variability in intraseasonal and synoptic scales

From the aspect of observations, the intraseasonal activities, such as MJO, normally are more active in boreal winter than in boreal summer. However, from the results of averaged HFI in intraseasonal scale, intraseasonal disturbance may be much stronger in SO(0) than in FM(+1). Here the evolutions of intraseasonal disturbances in these two periods will be shown as follows.

In this section, we will mainly show the spatial and temporal features of the HF zonal variability in both intraseasonal and synoptic scales. From the distribution of the standard deviation of intraseasonal zonal wind at 850 hPa (figure not shown), the box over (5° S–5° N, 150° E–170° E) in the WEP region exhibits the maximum standard deviation in both SO(0) and FM (+1), we hence utilized

the time series of the intraseasonal zonal wind anomaly at 850 hPa averaged over the reference box (5° S–5° N, 150° E–170° E) as an index to conduct the lead-lag regression analysis. Figure 4 shows the lead-lag regression maps of the OLR anomaly field and the wind anomaly field at 850 hPa against the index of the intraseasonal zonal wind anomaly at 850 hPa averaged over the reference box. For the pre-peak stage, the evolution maps of intraseasonal OLR anomaly and wind anomaly at 850 hPa from day − 15 (lag − 15d) to day 15 (lag15d) relative to the peak of westerly anomaly at day 0 (lag0d) are presented in the left column of Fig. 4. At day 0, the intraseasonal activity is characterized by a strong westerly wind along the equator, associated with the convective center locating to the center of westerly zonal wind and a pair of cyclonic wind anomalies with respect to the equator. Such structure fits the classical MJO structure that many previous studies have demonstrated. The evolution maps show that the convective center of this type of intraseasonal variability exhibits a northward propagation feature. The time-latitude diagram in Fig. 5 displays the slice of OLR anomaly averaged from 130° E to 180°, which further confirms that the convective signals (the shading with blue color) exhibit an obvious northward propagation feature. This northward propagation feature is similar to boreal summer intraseasonal oscillation (BSISO), the intraseasonal mode in boreal summer (Sikka et al. 1980; Wang and Rui 1990; Jiang et al. 2004). It may result from that this kind of intraseasonal variability during SO(0) seems to be similar to the intraseasonal variability during boreal summer, and

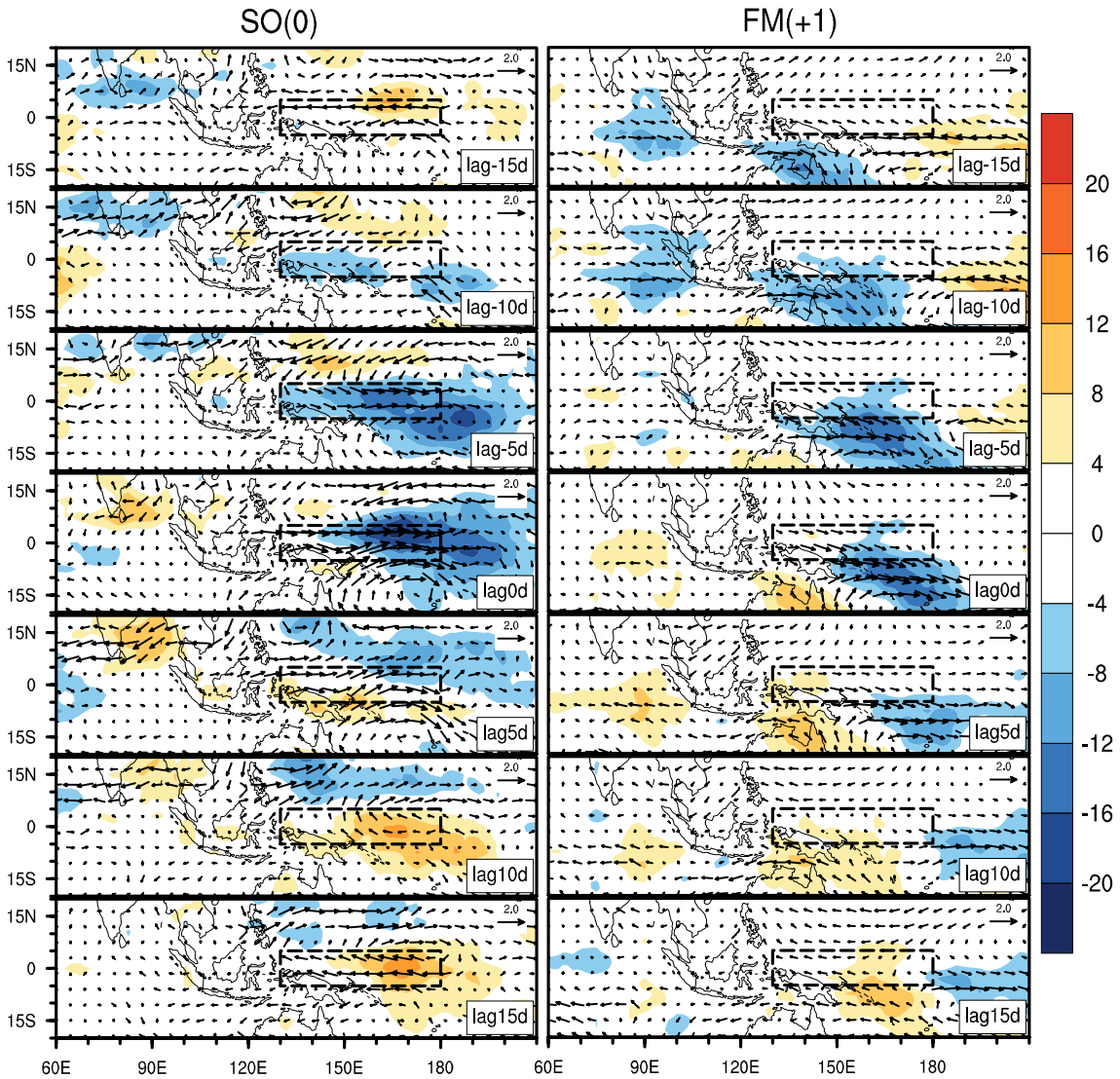

Fig. 4 Lead-lag regression maps of intraseasonal (20–90 days) zonal wind at 850 hPa averaged in (5° S–5° N, 150 °E–170° E) on OLR (W m^{-2}, shaded) and wind field (m s^{-1}, vectors) at 850 hPa during EP El Niños. The black boxes highlight the WEP region. The left column shows the evolution in SO(0), with a 5 days interval, while the right column shows that in FM(+1)

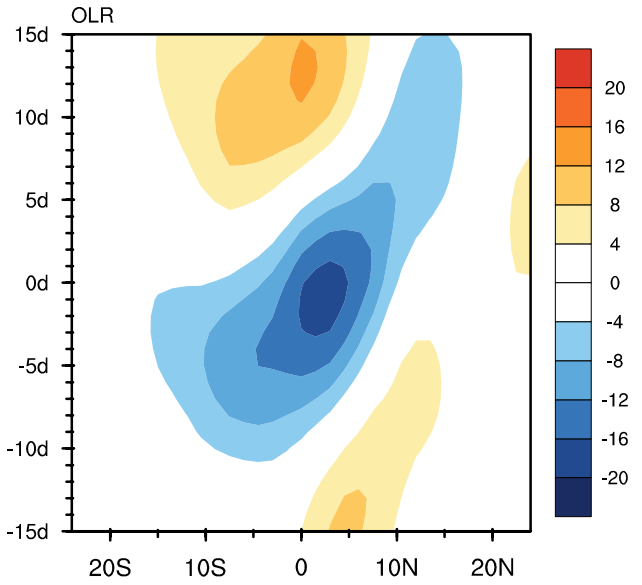

Fig. 5 Time-latitude diagram representing evolutions of OLR in Fig. 4, averaged from 130° E to 180°

its northward propagation feature during SO(0) is closer to BSISO than classical MJO, accordingly.

The right column of Fig. 4 displays the regression maps of the intraseasonal signals in FM(+1) during EP El Niños. The main structure of the intraseasonal variability activity can be seen at lag0d in FM(+1). It is noted that the center of westerly zonal wind anomaly and OLR anomaly is located to the south of the equator. Such southward shift may result from the seasonal cycle (Harrison and Vecchi 1999; Vecchi 2006; McGregor et al. 2012). The climatological wind speed south of the equator seasonally weakens during boreal winter and early spring, which leads to anomalous Ekman pumping at the boundary layer and a reduced surface momentum damping. This allows the southward shift of the anomalous zonal wind and convection. More details could be seen in McGregor et al. (2012). The lead-lag regression maps further show that the intraseasonal activity in FM(+1) also exhibits a significant eastward propagation feature, that is, the center of convection shifting from 135° E at day − 15 to 175 °E at day 5. The standard deviation of the zonal wind anomaly at 850 hPa and OLR anomaly averaged in the WEP region during the SO(0) stage as presented in the left column is, respectively, 4.39 m s^{-1} and 0.43 W m^{-2}, while the counterparts during the FM(+1) stage as presented in right column is, respectively, 2.66 m s^{-1} and 0.29 W m^{-2}. Based on both the magnitudes of the intraseasonal OLR anomaly and zonal wind anomaly between the two stages, it is obvious that the intraseasonal variability in SO(0) is significantly stronger than that in FM(+1) during the EP El Niños.

As we know, the equatorial waves with synoptic scale (0–20 days) have their respective kinds of spatial–temporal structures, thus the differences of the intensity of different equatorial waves between SO(0) and FM(+1) may be various. Here the different atmospheric equatorial waves' components were obtained following Wheeler and Kiladis (1999). Based on the wavenumber-frequency spectrum of the zonal wind around the equator, five components of synoptic disturbances are filtered, including eastward internal-gravity wave, westward internal-gravity wave, equatorial Rossby wave, Kelvin wave and MRG. The HFI of anomalous zonal wind and OLR for these five components during SO(0) and FM(+1) and the difference between these two stages are shown in Fig. 6. As seen from Fig. 6c, the difference in the HF zonal wind variability with synoptic scale between SO(0) and FM(+1) primarily arises from the differences in the equatorial Rossby wave and MRG components, while the difference in the Kelvin wave component makes a negative contribution and the differences in the eastward internal-gravity and westward internal-gravity waves make negligible contributions. Also seen from Fig. 6d, the difference in the HF OLR anomaly with the synoptic time scale between SO(0) and FM(+1) is mainly attributed to the differences in the equatorial Rossby wave and MRG components. The results based on the perspective of the OLR anomaly confirm that these two types of Rossby waves (say, equatorial Rossby wave and MRG) are stronger in SO(0) than those in FM(+1) during EP El Niños. This indicates that the differences in the intensities of equatorial Rossby wave and MRG between SO(0) and FM(+1) are the main contributors to the fact that the intensity of zonal wind variability at synoptic time scale is stronger in pre-peak stage than that in post-peak stage.

Next, we investigate the difference in the spatial–temporal characteristics of equatorial Rossby wave and MRG between these two episodes. In order to demonstrate the evolution features of equatorial waves, the method proposed by Waliser et al. (2009) to calculate the Real-time Multivariate MJO (RMM) index is adopted here. Specifically, we firstly applied multivariate empirical orthogonal function (MEOF) analysis to the OLR and wind anomalies at 850 hPa associated with equatorial Rossby wave component in SO(0) in WEP region. Then we obtained the first and second EOF eigenvectors, which accounted for 21.2 and 20.7% of the total variance, respectively. As the variance of th first and second EOF eigenvectors are close to each other and the their spatial patterns exhibit the consecutive evolution feature (not shown), it is hence suggested that the eigenvalues of these two modes (RMM_1 and RMM_2) could represent both the amplitudes and propagation feature of equatorial Rossby wave, analogous to that used in previous MJO studies. Likewise, an index describing the amplitudes, $\sqrt{RMM_1^2 + RMM_2^2}$, is calculated; then each peak whose amplitude is larger than one standard deviation of the index is defined as lag0d. The

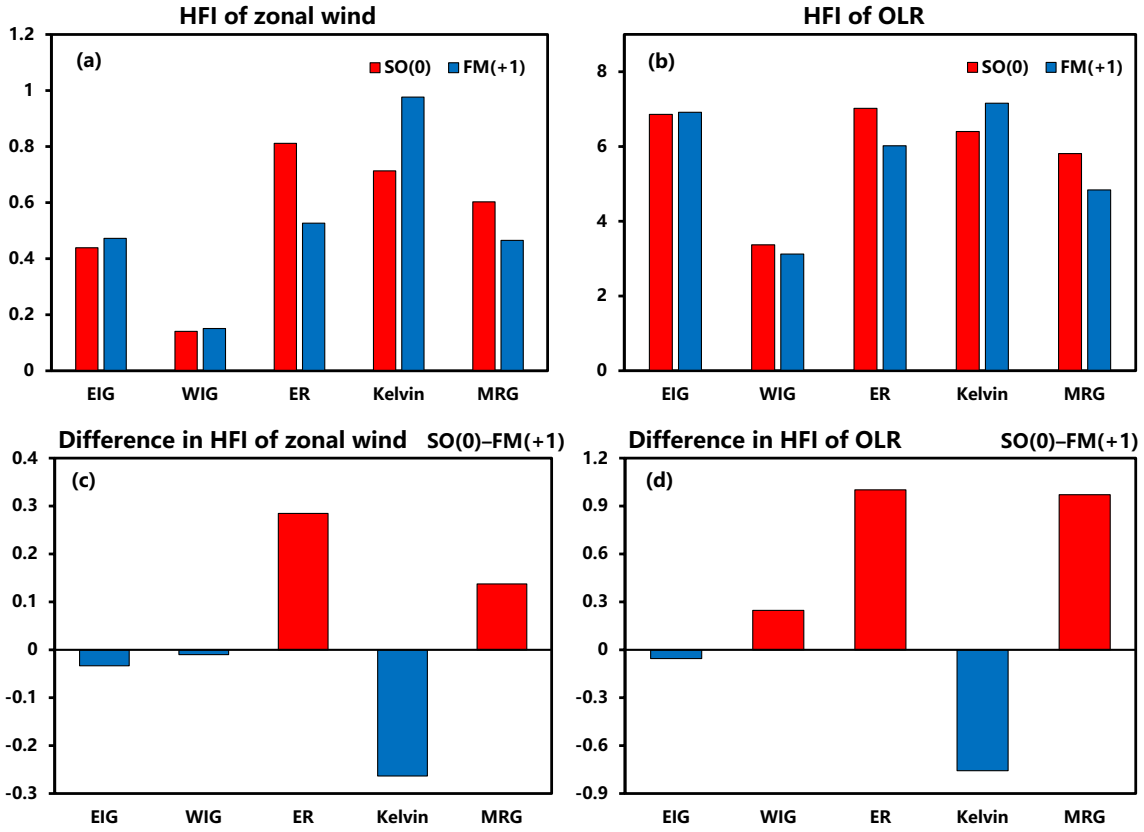

Fig. 6 The HFI of the **a** anomalous zonal wind and **b** OLR averaged in the WEP region from the five synoptic equatorial waves (eastward internal gravity wave, EIG; westward internal gravity wave, WIG; equatorial Rossby wave, ER; Kelvin wave, Kelvin; Mixed Rossby gravity wave, MRG) in SO (0) and FM (+1) during EP El Niños. **c**, **d** same as **a**, **b** but for their difference between these two stages

corresponding composite OLR and wind anomalies at 850 hPa associated with the equatorial Rossby wave component from day − 3 to day 3 during SO(0) are displayed in the left column of Fig. 7. At day 0 (i.e., lag0d), the westerly wind anomalies exist in the WEP region, with a pair of cyclonic wind anomalies centered at 20 °N and 5 °S. The convective region (i.e., the OLR disturbance clustering) appears to the north of the equator, locating to the northeast of the westerly wind anomaly. As seen in the spatial patterns in day − 3 and day 3, the OLR and wind anomalies exhibit a westward propagation feature, which confirms the features of the equatorial Rossby wave structure. As displayed in the right column of Fig. 7, the composite equatorial Rossby wave component in FM(+1) exhibits similar features to that in SO(0). For instance, the composite maps at different lead-lag days also indicate an obvious westward propagation feature. The difference in the spatial structure of equatorial Rossby wave between SO(0) and FM(+1) mainly lies in that the twin cyclones are not clear with respect to the equator at lag0d, whereas significant cyclonic circulation and convective region exist to the south of the equator.

The major difference in the equatorial Rossby wave between SO(0) and FM(+1) lies in their different intensities. In particular, the standard deviation of zonal wind in the WEP region in SO(0) is about 0.23 m s^{-1}; while the counterpart in FM(+1) is about 0.12 m s^{-1}, which reaches only half of that in SO(0). This suggests that the equatorial Rossby wave is more active in SO(0) than that in FM(+1) during EP El Niño, which partly contributes to the difference in the intensity of HF zonal wind variability.

We further adopted the method used above to further analyze the difference in the MRG component between the two episodes. The first two eigenvectors account for 12.9 and 12.5% of total variance in SO(0), and the counterparts are 11.1 and 11.0% in FM(+1). Although the percentages of the variance are less than those for the equatorial Rossby wave, the characteristic of MRG could still be seen clearly in eigenvectors' maps. The left column of Fig. 8 displays the composite OLR anomaly and wind anomaly filed at 850 hPa associated with MRG component from day − 2 and day 2 in SO (0). At day 0 (i.e., lag0d), an obvious clockwise circulation centered near the equator exists to the east of the WEP region, and the associated convection region exists to the northwest of the cyclonic circulation. As shown in the composite maps at different lag days, the cross-equator circulation and the convective region indicate a westward

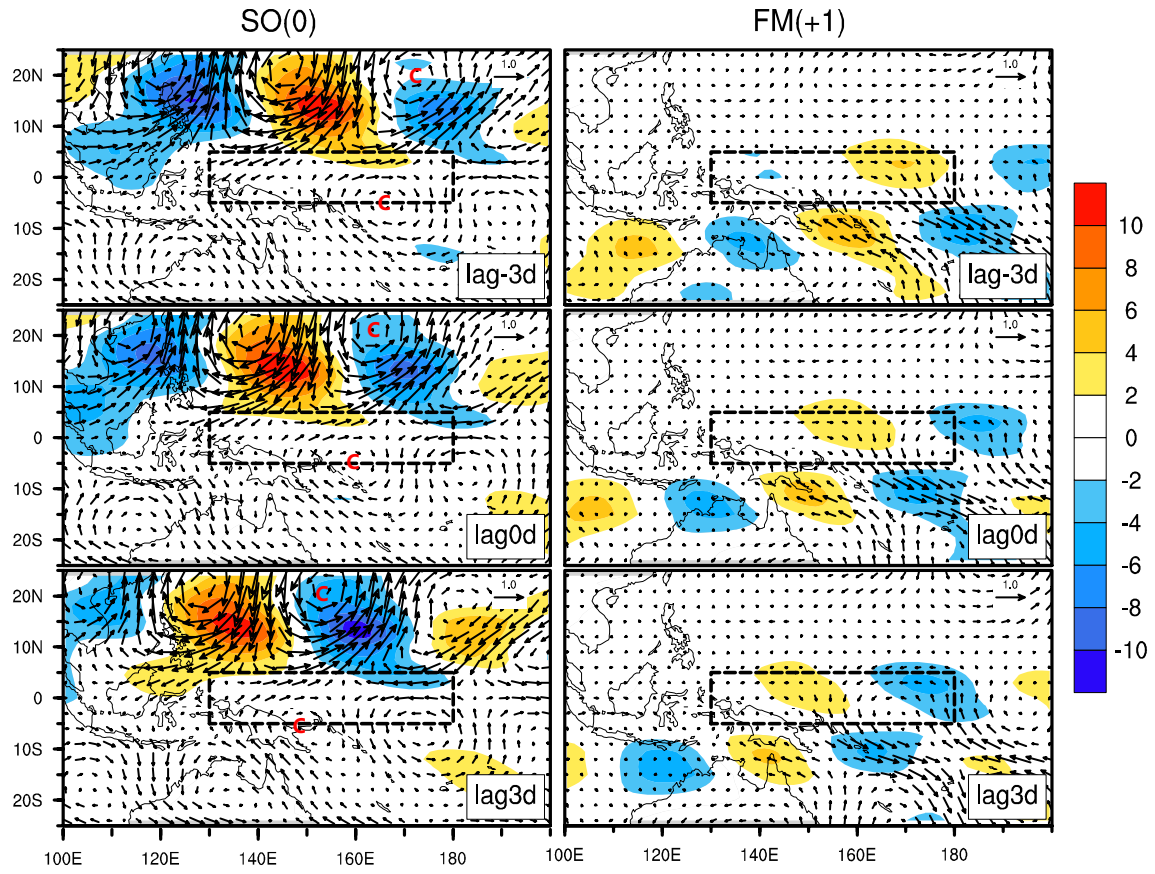

Fig. 7 Composite maps of equatorial Rossby wave in western-central tropical Pacific, with wind field in 850 hPa (m s^{-1}, vectors) and OLR (W m^{-2}, shaded) in SO(0) and FM(+1) during EP El Niños. The locations of a pair of cyclones are marked by "C" during the evolution in SO(0). The black boxes denote the WEP region

propagation feature, which is consistent with the characteristics of MRG. The right column of Fig. 8 displays the spatial and temporal evolution of the MRG component in FM(+1). The feature of MRG is still obvious, although the OLR anomaly and wind anomaly fields exhibit weaker and the corresponding circulation shifts further south compared to that in SO(0). As seen from the lead-lag maps, the temporal evolution of the convection and wind anomalies also show a modest westward propagation feature. Unlike the theoretical structure which obviously shows an anti-symmetric cross-equatorial flow (Matsuno 1966), the MRG component here exhibited slightly slant, so that the cross-equatorial flow contains zonal wind anomaly component. When comparing the composite results between SO(0) and FM(+1), the intensity of the MRG component is stronger in SO(0) than that in FM (+1) during EP El Niño, which also make a positive contribution to the difference in the intensity of HF zonal wind variability between the two episodes.

In this section, we have shown the spatial–temporal structures of the intraseasonal and synoptic zonal wind variabilities in SO(0) and FM(+1) during EP El Niños. As components of the synoptic variability, the equatorial Rossby wave and MRG appear to be indeed larger in SO(0) than those in FM(+1), although the background SST in these two periods is similar.

5 Causes for the different HF variabilities between SO(0) and FM(+1)

In this section, we will investigate the causes for the differences in the intensity of high-frequency disturbances between SO(0) and FM(+1), especially for the EP El Niño cases.

Previous study (e.g. Wang et al. 1996) has documented that the vertical wind shear has great influences on the growth of synoptic disturbances, i.e., for the equatorial Rossby wave and MRG. We first examined the vertical wind shear (here is defined as the difference between zonal wind at 200 hPa and 850 hPa) in SO(0) and FM(+1). As the climatological state of the wind vertical shear in SO and FM is close to each other (about − 4 ms^{-1}, not shown), we further examined whether there is a significant difference in the vertical wind shear at the interannual time scale (because

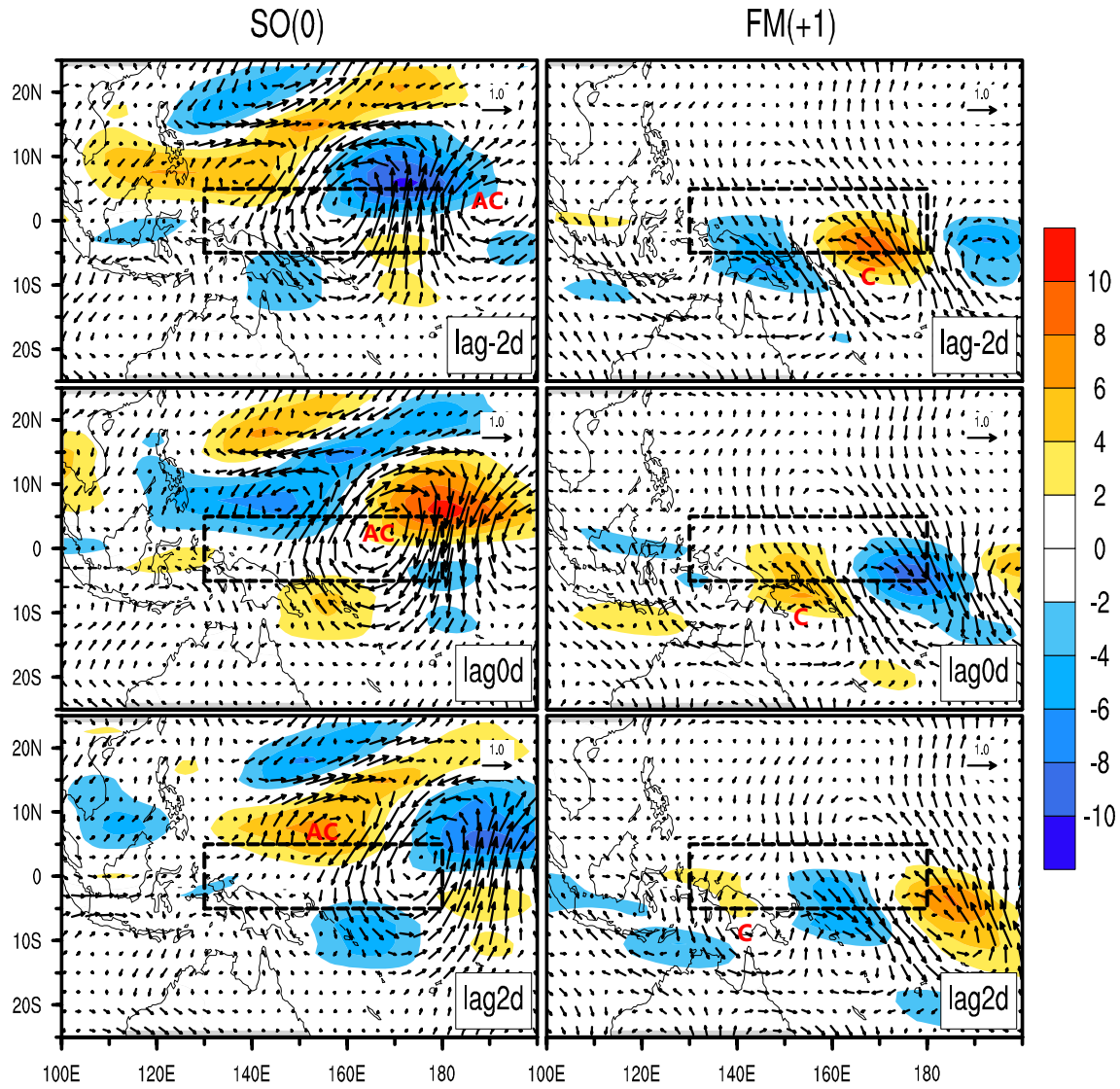

Fig. 8 Composite maps of MRG in western-central tropical Pacific, with wind field in 850 hPa (m s^{-1}, vectors) and OLR (W m^{-2}, shaded) in SO(0) and FM(+1) during EP El Niños. The centers of anti-cyclones (cyclones) are marked by "AC" ("C") during SO(0) (FM(+1)). The black boxes denote the WEP region

the interannual time scale can also be regarded as the background state for the synoptic variance). Figure 9a, b show the distribution of vertical shear over the equatorial Pacific in SO(0) and FM(+1). It is found that in the stage of SO(0), easterly wind shear mainly dominates from the dateline to the WEP region; in contrast, the easterly wind shear seems to shift eastward, and the vertical shear exhibits nearly zero in the WEP region in the stage of FM(+1). As seen from the difference map (Fig. 9c), there is a pronounced easterly wind shear in the WEP region during SO(0) compared to that in FM(+1). Figure 10 further shows the vertical profiles of the interannual anomaly of zonal wind averaged over WEP region in SO(0) and FM(+1). Clearly, the composite zonal wind anomaly (see red curve in Fig. 10) exhibits a great easterly wind shear in SO(0) (Fig. 10a), while the vertical shear is marginal in FM(+1). The profiles of the anomalous zonal wind derived from the three EP El Niños (see black curves in Fig. 10) further confirm that a greater easterly wind shear in SO(0) than that in FM(+1) holds for each case analyzed in this study. In particular, the anomalous easterly wind shear in SO(0) (about $-$ 10 m s^{-1}) is more than three times as large as that in FM(+1) (about $-$ 3 m s^{-1}). Such significant difference in the vertical wind shear may play a role in determining the contrasting intensities of synoptic variability of zonal wind, which will be further verified by an ideal numerical experiment in next section.

To further investigate the physical factors responsible for the different vertical wind shear between SO(0) and

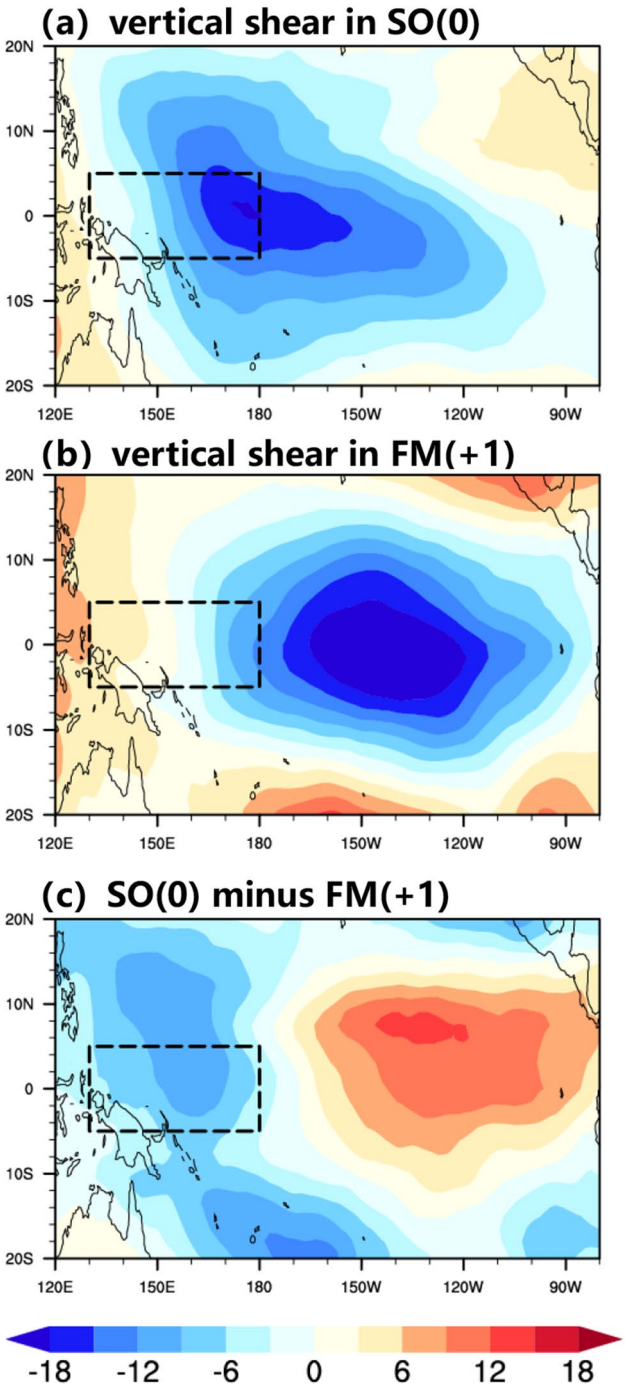

Fig. 9 Distributions of the vertical wind shear in **a** SO(0) and **b** in FM(+1) during EP El Niños, as well as **c** their difference (SO(0) minus FM(+1)). The black boxes denote the WEP region

FM(+1), we further present the specific spatial patterns of the wind anomaly fields at the upper-level and low-level in the two episodes. The composite maps of the anomalous winds at 200 and 850 hPa are presented by the vectors in Fig. 11. In SO(0), the anomalous westerly winds in the low-level are dominant in the WEP region (Fig. 11c); however, the easterly wind anomaly appears in the majority of the WEP region, and some weak westerly anomaly only appears near the east edge of WEP (Fig. 11d). Matching well with the wind anomaly fields in low-level, easterly wind anomaly appears in the upper-level over the entire WEP region in SO(0); however, easterly wind anomaly exists only in the east part of WEP region and westerly wind anomaly exists in the west part of WEP region in FM (+1) in the upper level. Such contrasting configuration of zonal wind anomalies in the upper-level and low-level between SO(0) and FM(+1) generates different vertical wind shear in the two episodes, as presented by the vertical profiles in Fig. 10.

In contrast, the spatial pattern of the SSTA in SO(0) bears a close resemblance to that in FM(+1) (see the shading in Fig. 11c, d). In SO(0), strong positive SST anomalies exist in the eastern equatorial Pacific, flanked by a horseshoe shape of negative SSTA anomalies in the western Pacific (Fig. 11c). As shown in Fig. 11d, a similar spatial pattern of SST is found in FM(+1). As mentioned previously, the magnitude of SSTA in the eastern equatorial Pacific and even the west–east gradient of SSTA at the equator in SO(0) and FM(+1) is close to each other. The different zonal wind anomalies in the upper-level and low-level between SO(0) and FM(+1) primarily arises from the different response of anomalous low-level wind to the similar SSTA forcing between pre-peak episode and post-peak episode of El Niño. In the post-peak episode, it is noted that an anomalous anticyclone in the western North Pacific (marked by "AC") should be responsible for the difference in low-level zonal wind anomaly. The anomaly circulation in the south edge of the anomalous anticyclone leads to the easterly anomaly in most of the WEP region. As documented by previous studies (Wang et al. 2002; Wu et al. 2017a, b), an anomalous anticyclone in the western North Pacific (marked by "AC") anticyclone only appears since the El Niño decay year's winter and can maintain to the ensuing summer. This causes the different responses of low-level wind anomaly to the similar SSTA forcing between pre-peak episode and post-peak episode, leading to the different vertical easterly wind shear in WEP region in the two episodes.

To investigate the causes for the difference of the intraseasonal variability between pre-peak episode and post-peak episode, we examined whether there is difference in the background states between the two episodes. Firstly, we checked the climatological mean states of the vertical velocity at 500 hPa (hereafter ω_{500}) and the specific humidity at 700 hPa. It is found that the difference in the climatological mean ω_{500} and the moisture between the long-term September–October mean and long-term February–March mean is negligible (not shown). Thus, we further examined that, in terms of the interannual time scale, whether there is significant difference in the ω_{500} and specific humidity anomalies. As shown in Fig. 12, the difference in the anomalous specific

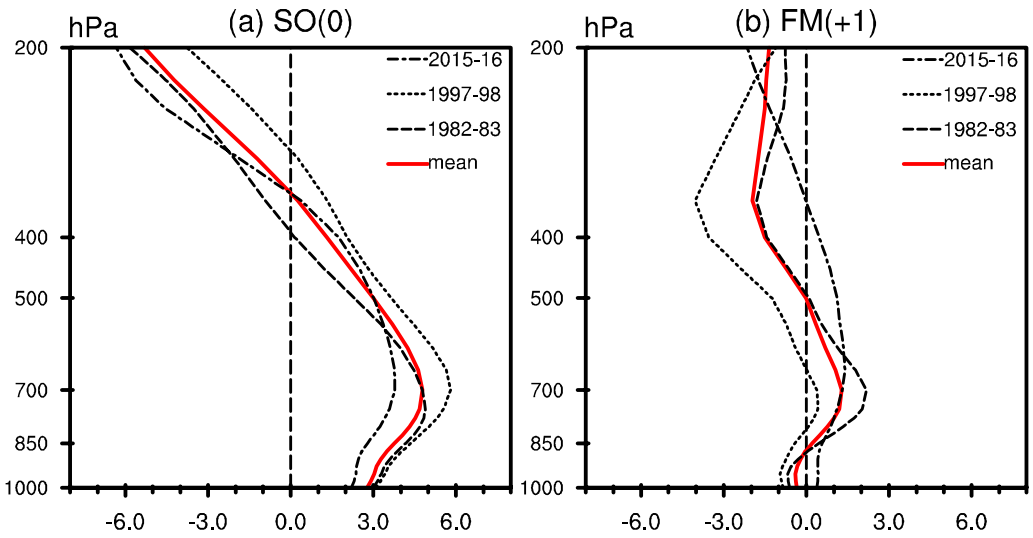

Fig. 10 Vertical wind profiles over the WEP region in SO(0) and FM(+1) for the EP El Niños

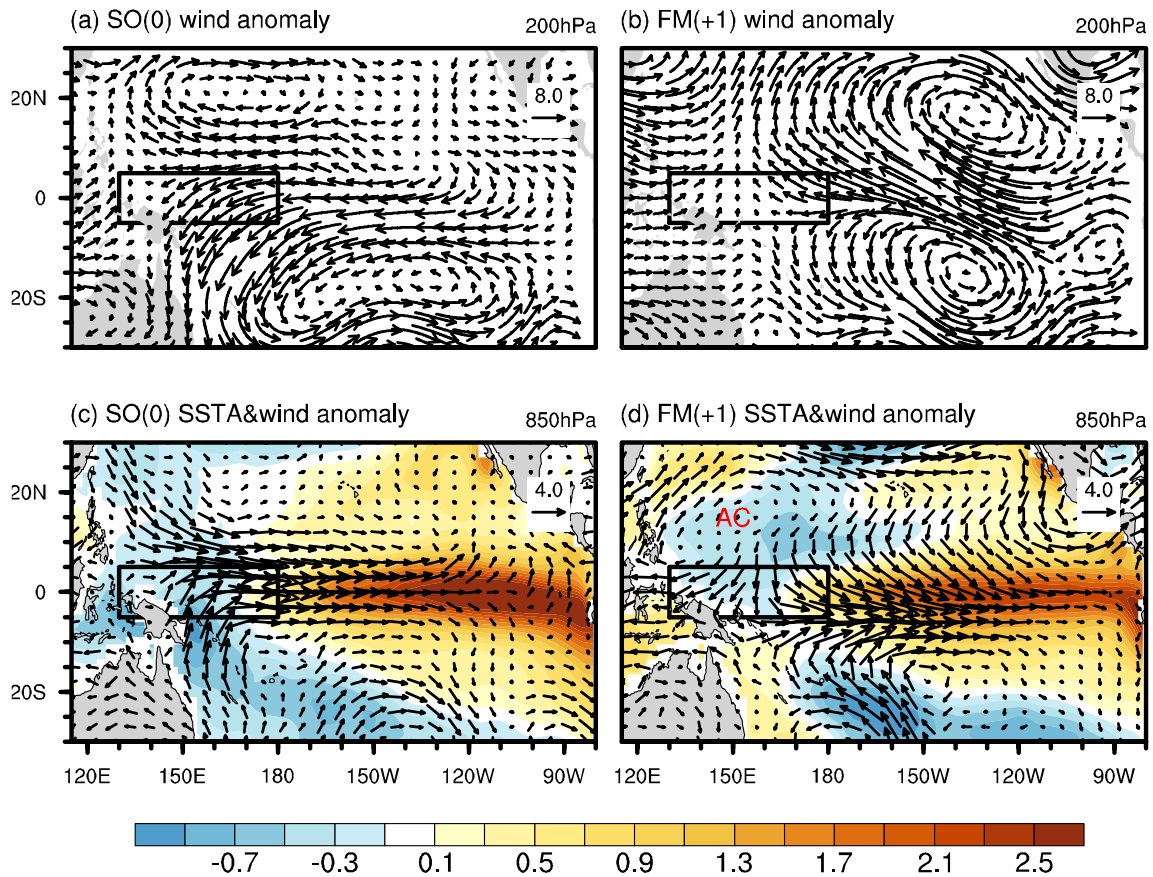

Fig. 11 Composites of **a**, **b** wind anomaly field (m s^{-1}, vectors) at 200 hPa, **c**, **d** anomalous SST (°C, shaded) and wind anomaly field (m s^{-1}, vectors) at 850 hPa in SO(0) and FM(+1) during EP El Niños. The black solid lines enclose the WEP region and 'AC' marks the location of anticyclone circulation over western North Pacific. The pattern correlation of SST anomalies between SO(0) and FM(+1) is 0.86, with 95% confidence level

humidity in low-level (see the contour) indicates that the moisture condition exhibits drier in FM(+1) than that in SO(0). Moreover, the difference in the anomalous vertical motion (see the shading) indicates there is more descending motion in FM(+1) compared to that in SO(0). As a result, the relatively dry condition and the relatively descending motion dominate in WEP region in FM(+1) compared to that in SO(0). This leads to a relatively unfavorable environmental condition for the intraseasonal perturbation's growth and development in FM(+1), and thus the intraseasonal variability in post-peak stage (i.e., FM(+1)) becomes weakened than that for the corresponding pre-peak stage (i.e., SO(0)) of EP El Niño events.

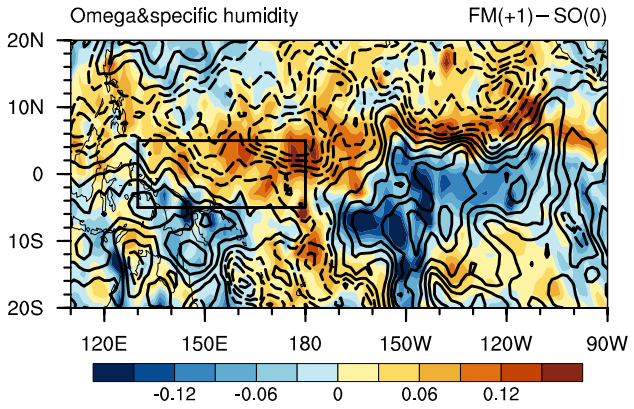

Fig. 12 The differences of vertical velocity (Pa s^{-1}, shade) and specific humidity (g g^{-1}, contour) anomalies (FM(+1) minus SO(0)) during EP El Niños. The black box denotes the WEP region

The differences in the interannual anomaly fields of ω500 and low-level moisture between the two episodes are also associated with the different response of the atmospheric circulation in the western North Pacific. Particularly, an anomalous anticyclone circulation in low-level occurs over the western North Pacific (WNPAC) in the post-peak stage while being absent in the pre-peak stage, even though the SSTA exhibits same magnitude and spatial pattern in SO(0) and FM(+1). The southern part of WNPAC induces anomalous divergence in low-level and anomalous descending motion in FM(+1) than that in SO(0), and thus the moisture in low-level is less in FM(+1) compared to SO(0). Consequently, the vertical motion and moisture conditions in FM(+1) is relatively unfavorable for the intraseasonal variability's development compared to that in SO(0), leading to the weaker intraseasonal variability in FM(+1) than that in SO(0).

Additionally, the conditions of the atmospheric stability may also play a role in influencing the intensity of high-frequency variabilities. Figure 13 displays the composited vertical profiles of the differences of two thermodynamic variables between SO(0) and FM(+1), averaged in region researched, with blue shades representing the standard deviation of each level. Figure 13a displays the vertical profile of the difference of the troposphere temperature anomaly averaged over WEP. In the low-level of troposphere (below 850 hPa), the difference of the temperature anomaly between SO(0) and FM(+1) is negligible. In contrast, the difference of the temperature anomaly above 850 hPa is negative, which indicates that high-level atmosphere is colder in SO(0) than that in FM(+1). The larger lapse rate of temperature anomaly in SO(0) than that in

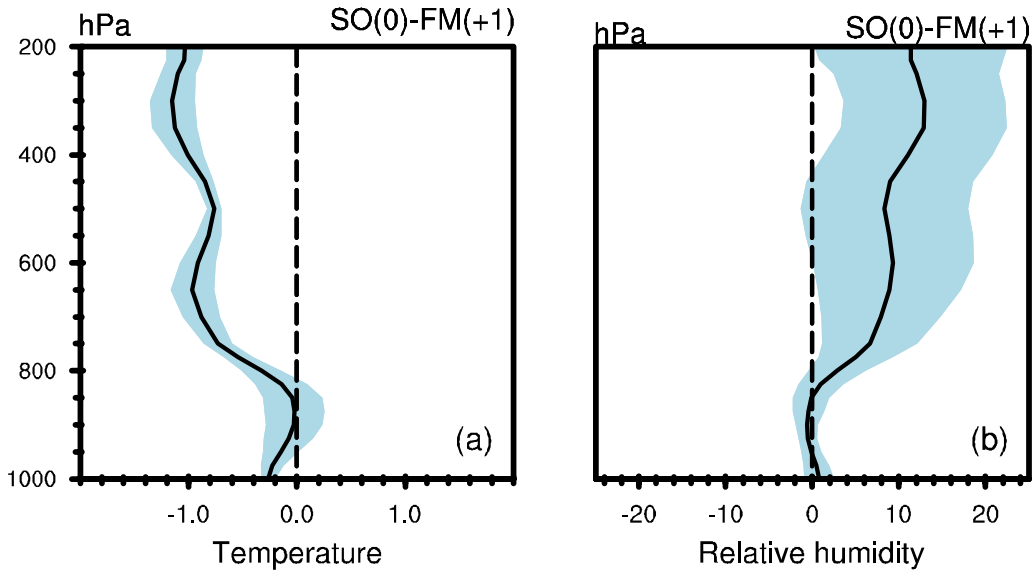

Fig. 13 Vertical profiles of the difference [SO(0) minus FM(+1)) of **a** temperature and **b** relative humidity averaged in the WEP region during EP El Niños. The blue shading represents the standard deviation among the EP El Niño cases

FM(+1) indicates a more unstable environment for atmosphere exists in SO(0) from the aspect of static instability. Figure 13b shows the same vertical profiles but for relative humidity. It is found that the moisture difference is slightly negative below 850 hPa but positive above 850 hPa. This suggests that the air in high-level troposphere in SO(0) is moister than that in FM(+1), indicating the atmosphere in SO(0) is more unstable than that in FM(+1). From the perspective of the temperature anomaly and moisture anomaly, the environment of troposphere in SO(0) is more unstable that in FM(+1), which may make the high-frequency variabilities to be easier to grow and develop in SO(0) than that in FM(+1). The contribution of atmospheric stability to the perturbation's growth will be further examined by an ideal numerical experiment in next section.

In this section, we found that the difference in synoptic variability between SO(0) and FM(+1) is primarily attributed to the difference in vertical wind shear. The stronger vertical easterly wind shear in SO(0) than that in FM(+1) plays an important role in causing the stronger synoptic equatorial Rossby wave and MRG, which contributes to the stronger synoptic variability in WEP region in SO(0). On the other hand, the weakened intraseasonal variability in FM(+1) compared to that in SO(0) results from the drier atmosphere and more dominant atmospheric descending motion over the WEP region in FM(+1) than that in SO(0). The weakened easterly wind shear, drier atmosphere and more descending motion in FM(+1) in the WEP region are due to the occurrence of the WNPAC during the post-peak phase of El Niño. Anomalous easterly wind exists along the south edge of such anomalous anticyclone, leading to the weaker vertical easterly wind shear in FM(+1) than that in SO(0). The southern part of WNPAC induces anomalous divergence in the low-level atmosphere and anomalous descending motion in WEP in FM(+1) than that in SO(0), and hence less moisture in FM(+1) compared to SO(0). Consequently, the environmental fields in FM(+1) are less favorable for both the synoptic and intraseasonal variabilities to grow in FM(+1) than that in SO(+1). Besides, the atmospheric instability may also play a role in influencing the intensity of high-frequency disturbances. From the perspective of the vertical profiles of anomalous temperature and relative humidity, the atmosphere exhibits more unstable in SO(0) than that in FM (+1), and hence the more unstable atmosphere is more favorable for the HF variabilities' growth and development in SO(0) than that in FM(+1).

6 Numerical experiments

To verify the effects of vertical wind shears and atmosphere instability on high-frequency variability's intensity, the anomaly AGCM experiments were carried out. First, we examined the effects of vertical wind shears of mean zonal flow on the growth of equatorial initial perturbation. In the control run, the atmosphere is static. As analyzed in Sect. 4, the asymmetrical intensity of synoptic variability between SO(0) and FM(+1) is mainly contributed by equatorial Rossby wave and MRG. Thus, two different initial perturbations are prescribed with the structures roughly similar to these two types of equatorial waves (hereafter ER-like and MRG-like perturbations). Figure 14 shows the horizontal vorticity structures of the two types of initial perturbations. These perturbations are prescribed in the low-level troposphere (at $\sigma = 0.7$). Compared to the control run, three sensitivity experiments are conducted with different vertical zonal wind shears. In these three sensitivity experiments, both meridional and vertical velocity vanish and only the basic zonal wind keeps a thermal wind balance with temperature. In the first sensitivity experiment, an easterly wind shear of − 14 m/s with a linear vertical profile (i.e., − 7, − 3.5, 0, 3.5, 7 m/s for $\sigma = 0.1, 0.3, 0.5, 0.7, 0.9$) is set (hereafter 14ES run). In the second experiment, a westerly wind shear of 14 m/s is applied (hereafter 14WS run). In the third experiment, the vertical wind shear is − 7 m/s (hereafter 7ES run). Perturbation kinetic energy vertically integrated for the whole atmosphere column averaged around the tropical region (30° S–30° N) is used here to represent the intensity of perturbations.

Figure 15a shows the evolutions of perturbation kinetic energy in these four experiments with the ER-like initial perturbation. In all of these three sensitivity experiments with vertical wind shears (colored lines), perturbations grow faster than control run (black line). It is clear that the perturbation grows fastest in 14ES run (blue line), which is much larger than that derived from 14WS run (brown line), even though both of them have the same magnitude of vertical shear. In 7ES run (red line), in which the vertical wind shear is half of that in 14ES run, the growth rate is much smaller than that in 14ES, but is very close to that of 14WS. Similar results could be seen in experiments using MRG-like initial perturbation, as shown in Fig. 15b. This series of experiments indicates that the easterly wind shear is more favorable for the tropical perturbation growth than the westerly wind shear, and the larger easterly wind shear corresponds to the larger growth rate of perturbation.

To examine the influence of atmosphere instability on the growth of equatorial perturbation, another sets of experiments were conducted. In the first experiment, the atmosphere is static and the temperature vertical profile is equal to that of FM(+1) in EP El Niños (hereafter FM run). In the second experiment, the temperature vertical profile is equal to that of SO(0) in EP El Niño (hereafter SO1 run). The third experiment (hereafter SO2 run) is same as SO1 run, except that the difference of the temperature profile is double (i.e., the temperature profile for the third experiment

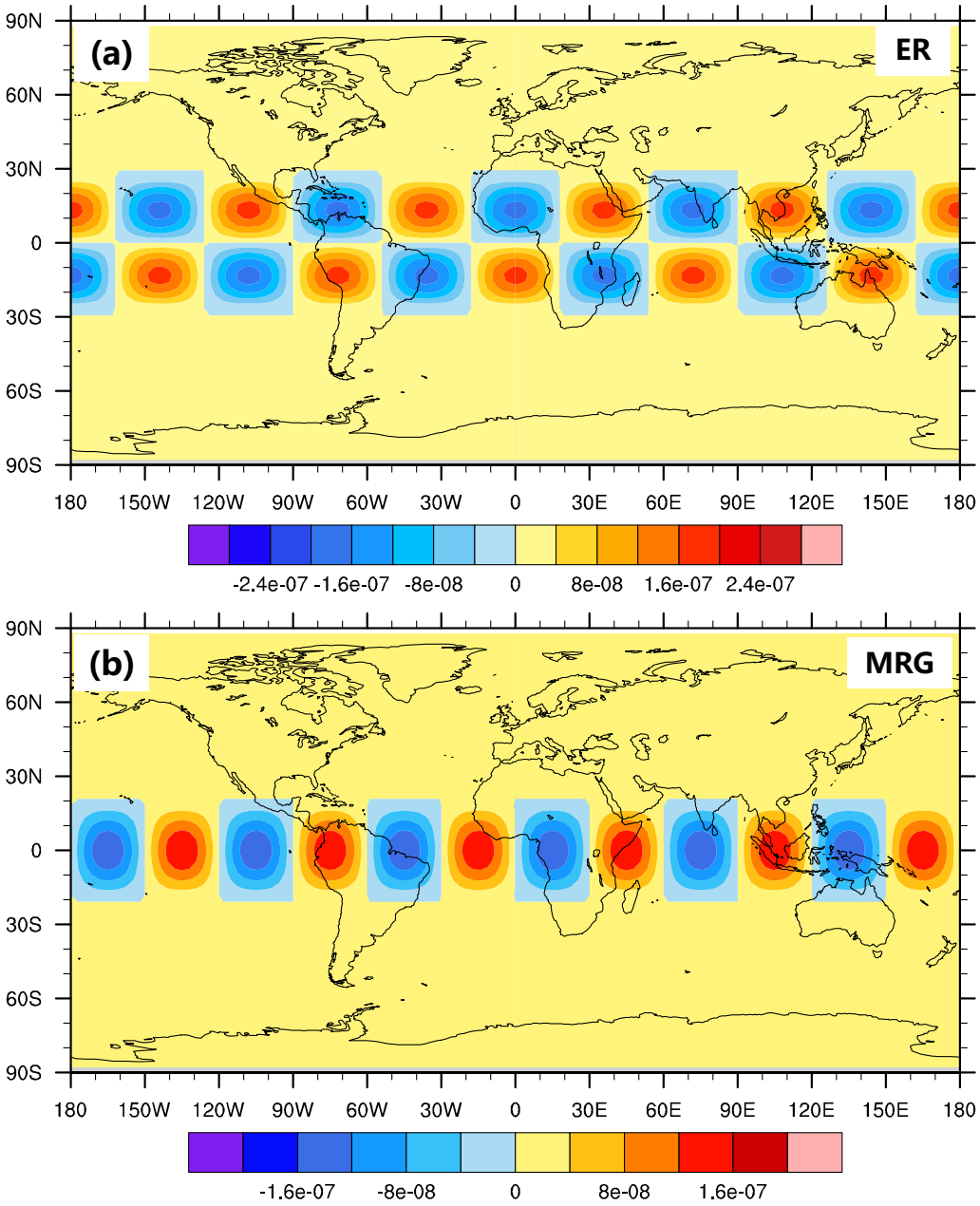

Fig. 14 The horizontal patterns of vorticity of the two initial perturbations, whose structures are roughly similar to **a** the equatorial Rossby wave and **b** MRG

is the summation of that for FM run and the additional part equal to that twice as much as the difference between SO1 run and FM run. Figure 16a displays the evolution of the perturbation kinetic energy in experiments with ER-like initial perturbation. The perturbation growth rate in SO1 run is larger than that in FM run. With the doubled difference of temperature profile, the difference of the perturbation growth rate between SO2 run and FM run is nearly twice as much as that between SO1 run and FM run. This indicates that a more unstable atmosphere plays a role in contributing to the faster perturbation growth rate and the stronger intensity of the synoptic perturbation. Figure 16b shows the similar results in experiments with MRG-like initial perturbation. However, the impact of temperature profiles' changes on the perturbation's growth rate seems weaker than that of vertical wind shear, when comparing the variation of the perturbation kinetic energy shown in Figs. 15 and 16.

These two groups of experiments confirm that both changes of vertical wind shears and temperature profiles could influence the growth of perturbation, and the vertical

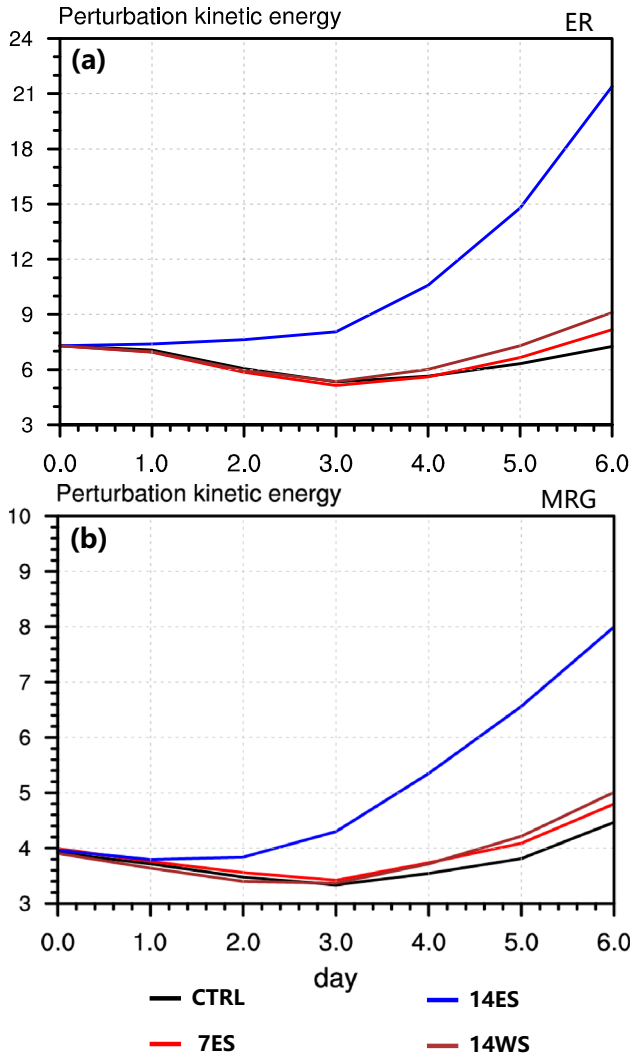

Fig. 15 Evolutions of the perturbation kinetic energy in the two sets of sensitivity experiments using **a** equatorial Rossby wave and **b** MRG as the initial perturbation respectively. In particular, different vertical wind shears have been prescribed: control run (no vertical shear, black line), 14ES run (easterly wind shear that equals to 14 m s^{-1}, blue line), 14WS run (westerly wind shear that equal to − 14 m s^{-1}, brown line) and 7ES run (easterly wind shear that equals to 7 m s^{-1}, red line)

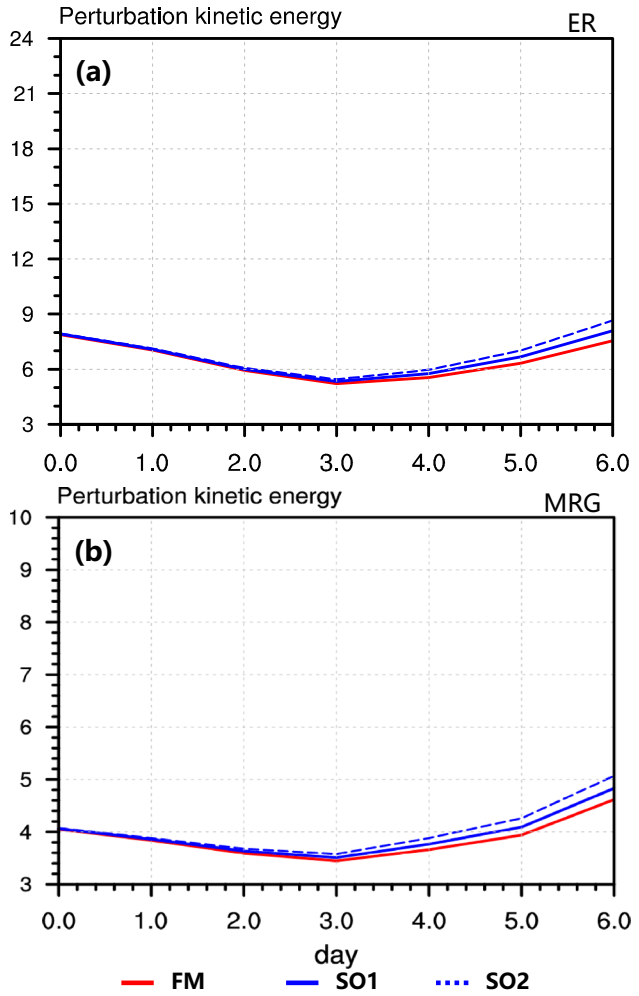

Fig. 16 Evolutions of the perturbation kinetic energy in the sensitivity experiments using **a** equatorial Rossby wave and **b** MRG as the initial perturbation respectively. Here the different temperature profiles are prescribed in these experiments: FM run (red solid), SO1 run (blue solid), and SO2 run (blue dash)

wind shear plays a more important role on enhancement of HF variabilities over the tropical region. Recalling the observational distribution of vertical shear in Sect. 5, the easterly wind shear in SO(0) is much pronounced compared to that in FM(+1) over the WEP. Combining the observational evidence and the numerical experiment results, it is argued here that the greater easterly wind shear and more unstable atmosphere in SO(0) than those in FM (+1) causes the stronger HF zonal wind variability in SO(0) over the WEP region.

7 Summary and discussion

Previous studies have pointed out that the HF zonal wind variability in the WEP region with period less than 90 days plays a vital role in affecting the interannual SSTA variability; and the HF zonal wind variability, in turn, is modulated by the change of SST in the equatorial Pacific. The present study found a large asymmetry in the intensity of the HF zonal wind variability between the pre-peak stage and post-peak stage of El Niño, although the magnitude of the SSTA in the eastern equatorial Pacific and the overall SSTA pattern in the tropical region during the two stages are almost the same. This leads to analyses on the specific components that contribute to the difference of the HF variability between the pre-peak stage and post-peak stage and then on investigation of the physical causes at work.

We decomposed the HF zonal wind variability into two different time scales—the intraseasonal variability (20–90 days) and synoptic variability (< 20 days). The results show that the differences of the zonal wind variability in these two time scales make positive contributions to the asymmetric intensity of HF zonal wind variability. Based on the lead-lag regression analysis, we then showed the spatial–temporal structures of the intraseasonal variability. We found that the zonal wind and OLR anomalies in the intraseasonal time scale in SO(0) are indeed stronger than those in FM(+1). According to the Wheeler-Kiladis space–time spectral analysis, we then revealed that different intensities of the synoptic disturbances between SO(0) and FM(+1) primarily arises from the contrasting intensities of MRG and equatorial Rossby wave components between SO(0) and FM(+1). Imitating the method used to calculate RMM index in MJO studies, we also presented the spatial–temporal structures of the wind and OLR anomalies of MRG and equatorial Rossby wave components, both of which exhibit the classic features of Rossby waves. The corresponding zonal wind and OLR fields of both MRG and equatorial Rossby waves further confirmed that both of them exhibit stronger intensities in SO(0) than in FM (+1).

Our analysis suggests that the difference in synoptic variability of zonal wind disturbances between SO(0) and FM(+1) is primarily attributed to the difference in vertical wind shear. The stronger vertical easterly wind shear in SO(0) than in FM(+1) plays a vital role in causing the stronger synoptic equatorial Rossby wave and MRG, which contributes to the stronger synoptic variability in the WEP region in SO(0). On the other hand, the weakened intraseasonal variability in FM(+1) compared to that in SO(0) is due to the drier atmosphere and more dominant atmospheric descending motion over the WEP region in FM(+1) than that in SO(0). The different vertical easterly wind shear, atmospheric moisture condition and vertical motion in the WEP region can be traced back to the different responses of atmospheric circulation to SSTA between SO(0) and FM(+1). During the post-peak phase of El Niño, an anomalous anticyclone in the low-level occurs in the western North Pacific, namely, WNPAC. Accordingly, an anomalous easterly wind exists along the south edge of such anomalous anticyclone, leading to weaker vertical easterly wind shear in FM(+1) than in SO(0). The southern part of the WNPAC induces anomalous divergence in the low level and anomalous descending motion in the WEP in FM(+1) than in SO(0), and hence there is less moisture in FM(+1) than in SO(0). Consequently, these environmental fields in FM(+1) are less favorable for both synoptic and intraseasonal variabilities to grow in FM(+1) than in SO(+1). Besides, the atmosphere exhibits more unstable in SO(0) than in FM (+1). The more unstable atmosphere is more favorable for the growth and development of HF disturbances, which also contributes to the stronger HF variability in SO(0) than in FM(+1).

We carried out several sets of sensitivity experiments to verify the effects of vertical wind shear and atmosphere instability on the synoptic variability, with the aid of an AGCM. Our experiment results show that the vertical wind shear plays a vital role in influencing the growth rate and development of the synoptic disturbance, and the atmospheric instability plays a secondary role. Specifically, the easterly wind shear is much favorable for the enhancement of the synoptic variability, that is, a larger easterly wind shear corresponds to a larger growth rate of HF perturbation. An unstable atmospheric environment can make the perturbation grow faster as well, but the impact of temperature profile is weak compared to the vertical wind shear's effect. It is worth noting that the SSTA does not play a direct role in determining the intensity of HF variability over the WEP during the evolution of El Niño events, which is largely determined by the environmental fields. However, these environmental fields such as vertical wind shear, moisture condition and vertical motion, are modulated by the SSTA forcing, indicating indirect but non negligible effects of the SSTA.

Acknowledgements This work was jointly supported by the NSFC Grants 41630423, National Key Research and Development Program on Monitoring, Early Warning and Prevention of Major Natural Disaster (2018YFC1506002), the Natural Science Foundation of Jiangsu Province (No. BK20190781), NSF AGS-2006553, NOAA NA18OAR4310298, NSF AGS-1643297, the General Program of Natural Science Foundation of Jiangsu Higher Education Institutions (19KJB170019), the LASG Open Project, the Open Fund of State Key Laboratory of Loess and Quartary Geology (SKLLQG1802), and the Startup Foundation for Introducing Talent of NUIST. This is SOEST contribution number 11096, IPRC contribution number 1456 and ESMC number 315.

References

Anderson DLT, McCreary JP, Anderson DLT, McCreary JP (1985) Slowly propagating disturbances in a coupled ocean-atmosphere model. J Atmos Sci 42:615–630. https://doi.org/10.1175/1520-0469(1985)042%3c0615:SPDIAC%3e2.0.CO;2

Anyamba EK, Weare BC (1995) Temporal variability of the 40–50-day oscillation in tropical convection. Int J Climatol 15:379–402. https://doi.org/10.1002/joc.3370150404

Ashok K, Behera SK, Rao SA, Weng H, Yamagata T (2007) El Niño Modoki and its possible teleconnection. J Geophys Res Oceans. https://doi.org/10.1029/2006jc003798

Batstone C, Hendon HH (2005) Characteristics of stochastic variability associated with ENSO and the role of the MJO. J Clim 18:1773–1789. https://doi.org/10.1175/JCLI3374.1

Boulanger J-P, Menkes C, Lengaigne M (2004) Role of high- and low-frequency winds and wave reflection in the onset, growth and termination of the 1997–1998 El Niño. Clim Dyn 22:267–280. https://doi.org/10.1007/s00382-003-0383-8

Cane MA, Zebiak SE (1985) A theory for El Niño and the Southern Oscillation. Science. https://doi.org/10.1126/science.228.4703.1085
Chen D et al (2015) Strong influence of westerly wind bursts on El Niño diversity. Nat Geosci 8:339
Chen L, Li T, Behera SK, Doi T (2016a) Distinctive precursory air-sea signals between regular and super El Niños. Adv Atmos Sci 33(8):996–1004. https://doi.org/10.1007/s00376-016-5250-8
Chen L, Yu Y, Zheng W (2016b) Improved ENSO simulation from climate system model FGOALS-g1.0 to FGOALS-g2. Clim Dyn 47(7):2617–2634. https://doi.org/10.1007/s00382-016-2988-8
Chen S, Wu R, Chen W, Yu B, Cao X (2016c) Genesis of westerly wind bursts over the equatorial western Pacific during the onset of the strong 2015–2016 El Niño. Atmos Sci Lett 17:384–391. https://doi.org/10.1002/asl.669
Chen L, Li T, Wang B, Wang L (2017) Formation mechanism for 2015/16 super El Niño. Sci Rep 7(1):2975. https://doi.org/10.1038/s41598-017-02926-3
Chen L, Wang L, Li T, Sun D-Z (2018) Contrasting cloud radiative feedbacks during warm pool and cold tongue El Niños. SOLA 14:126–131. https://doi.org/10.2151/sola.2018-022
Chen L, Wang L, Li T, Liu J (2019a) Drivers of reduced ENSO variability in mid-Holocene in a coupled model. Clim Dyn 52(9):5999–6014. https://doi.org/10.1007/s00382-018-4496-5
Chen L, Zheng W, Braconnot P (2019b) Towards understanding the suppressed ENSO activity during mid-Holocene in PMIP2 and PMIP3 simulations. Clim Dyn 53(1–2):1095–1110. https://doi.org/10.1007/s00382-019-04637-z
Chiodi AM, Harrison DE, Vecchi GA (2014) Subseasonal atmospheric variability and El Niño waveguide warming: observed effects of the Madden–Julian oscillation and westerly wind events. J Clim 27:3619–3642. https://doi.org/10.1175/jcli-d-13-00547.1
Clarke AJ, Van Gorder S, Clarke AJ, Gorder SV (1994) On ENSO coastal currents and sea levels. J Phys Oceanogr 24:661–680. https://doi.org/10.1175/1520-0485(1994)024%3c0661:OECCAS%3e2.0.CO;2
Davey MK (1989) A simple tropical moist model applied to the '40-day' wave. Quart J R Meteorol Soc 115:1071–1107. https://doi.org/10.1002/qj.49711548905
Dee DP et al (2011) The ERA-Interim reanalysis: configuration and performance of the data assimilation system. Quart J R Meteorol Soc 137:553–597. https://doi.org/10.1002/qj.828
Duchon CE (1979) Lanczos filtering in one and two dimensions. J Appl Meteorol 18(8):1016–1022. https://doi.org/10.1175/1520-0450(1979)018%3c1016:Lfioat%3e2.0.Co;2
Eisenman I, Yu L, Tziperman E (2005) Westerly wind bursts: ENSO's tail rather than the dog? J Clim 18(24):5224–5238. https://doi.org/10.1175/jcli3588.1
Fedorov AV, Hu S, Lengaigne M, Guilyardi E (2015) The impact of westerly wind bursts and ocean initial state on the development, and diversity of El Niño events. Clim Dyn 44:1381–1401. https://doi.org/10.1007/s00382-014-2126-4
Feng J, Lian T (2018) Assessing the relationship between MJO and equatorial Pacific WWBs in observations and CMIP5 models. J Clim 31(16):6393–6410. https://doi.org/10.1175/jcli-d-17-0526.1
Feng J, Li J, Zheng F, Xie F, Sun C (2016) Contrasting impacts of developing phases of two types of El Niño on Southern China rainfall. J Meteorol Soc Japan Ser. https://doi.org/10.2151/jmsj.2016-019
Feng J, Chen W, Li Y (2017) Asymmetry of the winter extra-tropical teleconnections in the Northern Hemisphere associated with two types of ENSO. Clim Dyn 48:2135–2151. https://doi.org/10.1007/s00382-016-3196-2
Fu M, Tziperman E (2019) Essential ingredients to the dynamics of westerly wind bursts. J Clim 32(17):5549–5565. https://doi.org/10.1175/jcli-d-18-0584.1
Gebbie G, Eisenman I, Wittenberg A, Tziperman E (2007) Modulation of westerly wind bursts by sea surface temperature: a semi-stochastic feedback for ENSO. J Atmos Sci 64(9):3281–3295. https://doi.org/10.1175/JAS4029.1
Guilyardi E et al (2009) Atmosphere feedbacks during ENSO in a coupled GCM with a modified atmospheric convection scheme. J Clim 22:5698–5718. https://doi.org/10.1175/2009JCLI2815.1
Gushchina D, Dewitte B (2012) Intraseasonal tropical atmospheric variability associated with the two flavors of El Niño. Mon Weather Rev 140(11):3669–3681. https://doi.org/10.1175/mwr-d-11-00267.1
Harrison DE, Vecchi GA (1997) Westerly wind events in the Tropical Pacific, 1986–1995. J Clim 10(12):3131–3156. https://doi.org/10.1175/1520-0442(1997)010%3c3131:Wweitt%3e2.0.Co;2
Harrison DE, Vecchi GA (1999) On the termination of El Niño. Geophys Res Lett 26:1593–1596. https://doi.org/10.1029/1999gl900031
Hayashi M, Watanabe M (2017) ENSO complexity induced by state dependence of westerly wind events. J Clim 30(9):3401–3420. https://doi.org/10.1175/jcli-d-16-0406.1
Held IM, Suarez MJ (1994) A proposal for the intercomparison of the dynamical cores of atmospheric general circulation models. Bull Am Meteor Soc 75(10):1825–1830. https://doi.org/10.4324/9780203073766
Hendon HH, Liebmann B, Glick JD (1998) Oceanic Kelvin waves and the Madden–Julian oscillation. J Atmos Sci 55(1):88–101. https://doi.org/10.1175/1520-0469(1998)055%3c0088:Okwatm%3e2.0.Co;2
Hendon HH, Zhang C, Glick JD (1999) Interannual variation of the Madden–Julian oscillation during austral summer. J Clim 12(8):2538–2550. https://doi.org/10.1175/1520-0442(1999)012%3c2538:Ivotmj%3e2.0.Co;2
Hendon HH, Wheeler MC, Zhang C (2007) Seasonal dependence of the MJO-ENSO relationship. J Clim 20(3):531–543. https://doi.org/10.1175/JCLI4003.1
Hong C-C, Li T (2009) The extreme cold anomaly over Southeast Asia in February 2008: roles of ISO and ENSO. J Clim 22(13):3786–3801. https://doi.org/10.1175/2009jcli2864.1
Hong C-C, Lee M-Y, Hsu H-H, Kuo J-L (2010) Role of submonthly disturbance and 40–50 day ISO on the extreme rainfall event associated with Typhoon Morakot (2009) in Southern Taiwan. Geophys Res Lett. https://doi.org/10.1029/2010gl042761
Horel JD, Wallace JM, Horel JD, Wallace JM (1981) Planetary-scale atmospheric phenomena associated with the Southern oscillation. Mon Weather Rev 109:813–829. https://doi.org/10.1175/1520-0493(1981)109%3c0813:PSAPAW%3e2.0.CO;2
Hu S, Fedorov AV, Lengaigne M, Guilyardi E (2014) The impact of westerly wind bursts on the diversity and predictability of El Niño events: an ocean energetics perspective. Geophys Res Lett 41(13):4654–4663. https://doi.org/10.1002/2014GL059573
Jiang XA, Li T (2005) Reinitiation of the boreal summer intraseasonal oscillation in the Tropical Indian Ocean. J Clim 18(18):3777–3795. https://doi.org/10.1175/JCLI3516.1
Jiang X, Li T, Wang B, Jiang X, Li T, Wang B (2004) Structures and mechanisms of the northward propagating boreal summer intraseasonal oscillation. J Clim 17:1022–1039. https://doi.org/10.1175/1520-0442(2004)017%3c1022:SAMOTN%3e2.0.CO;2
Kao H-Y, Yu J-Y (2009) Contrasting Eastern-Pacific and central-pacific types of ENSO. J Clim 22(3):615–632. https://doi.org/10.1175/2008jcli2309.1
Kessler WS, Kleeman R (2000) Rectification of the Madden–Julian oscillation into the ENSO cycle. J Clim 13(20):3560–3575. https://doi.org/10.1175/1520-0442(2000)013%3c3560:Rotmjo%3e2.0.Co;2

Kessler WS, McPhaden MJ, Weickmann KM (1995) Forcing of intraseasonal Kelvin waves in the equatorial Pacific. J Geophys Res Oceans 100(C6):10613–10631. https://doi.org/10.1029/95JC00382

Kug J-S, Jin F-F, Sooraj KP, Kang I-S (2008) State-dependent atmospheric noise associated with ENSO. Geophys Res Lett 35:L05701. https://doi.org/10.1029/2007GL032017

Kug J-S, Jin F-F, An S-I (2009a) Two Types of El Niño Events: cold Tongue El Niño and Warm Pool El Niño. J Clim 22(6):1499–1515. https://doi.org/10.1175/2008jcli2624.1

Kug J-S, Sooraj KP, Kim D, Kang I-S, Jin F-F, Takayabu YN, Kimoto M (2009b) Simulation of state-dependent high-frequency atmospheric variability associated with ENSO. Clim Dyn 32:635–648. https://doi.org/10.1007/s00382-008-0434-2

Larkin NK, Harrison DE (2005) On the definition of El Niño and associated seasonal average US weather anomalies. Geophys Res Lett. https://doi.org/10.1029/2005gl022738

Lau K-M (1981) Oscillations in a simple equatorial climate system. J Atmos Sci 38:248–261. https://doi.org/10.1175/1520-0469(1981)038%3c0248:OIASEC%3e2.0.CO;2

Lau WKM (2005) El Niño Southern oscillation connection. Springer, Berlin. https://doi.org/10.1007/3-540-27250-X_9

Lau K-M, Shen S (1988) On the dynamics of intraseasonal oscillations and ENSO. J Atmos Sci 45(12):1781–1797. https://doi.org/10.1175/1520-0469(1988)045%3c1781:Otdoio%3e2.0.Co;2

Lengaigne M et al (2004) Triggering of El Niño by westerly wind events in a coupled general circulation model. Clim Dyn 23(6):601–620. https://doi.org/10.1007/s00382-004-0457-2

Li T (2006) Origin of the summertime synoptic-scale wave train in the Western North Pacific. J Atmos Sci 63:1093–1102. https://doi.org/10.1175/JAS3676.1

Li G, Ren B (2012) Evidence for strengthening of the tropical Pacific Ocean surface wind speed during 1979–2001. Theoret Appl Climatol 107:59–72. https://doi.org/10.1007/s00704-011-0463-3

Lian T, Chen D, Tang Y, Wu Q (2014) Effects of westerly wind bursts on El Niño: a new perspective. Geophys Res Lett 41(10):3522–3527. https://doi.org/10.1002/2014GL059989

Lian T, Chen D, Tang Y, Liu X, Feng J, Zhou L (2018a) Linkage between westerly wind bursts and tropical cyclones. Geophys Res Lett 45(20):11431–411438. https://doi.org/10.1029/2018gl079745

Lian T, Tang Y, Zhou L, Islam SU, Zhang C, Li X, Ling Z (2018b) Westerly wind bursts simulated in CAM4 and CCSM4. Clim Dyn 50:1353–1371. https://doi.org/10.1007/s00382-017-3689-7

Liebmann B, Smith CA (1996) Description of a complete (interpolated) outgoing longwave radiation dataset. Am Meteorol Soc. https://doi.org/10.2307/26233278

Madden RA, Julian PR (1971) Detection of a 40–50 day oscillation in the zonal wind in the tropical Pacific. J Atmos Sci 28(5):702–708. https://doi.org/10.1175/1520-0469(1971)028%3c0702:Doadoi%3e2.0.Co;2

Madden RA, Julian PR (1972) Description of global-scale circulation cells in the tropics with a 40–50 day period. J Atmosp Sci 29(6):1109–1123. https://doi.org/10.1175/1520-0469(1972)029%3c1109:Dogscc%3e2.0.Co;2

Matsuno T (1966) Quasi-geostrophic motions in the equatorial area. J Meteorol Soc Japan Ser. https://doi.org/10.2151/jmsj1965.44.1_25

McGregor S, Timmermann A, Schneider N, Stuecker MF, England MH (2012) The effect of the south pacific convergence zone on the termination of El Niño events and the meridional asymmetry of ENSO. J Clim 25(16):5566–5586. https://doi.org/10.1175/jcli-d-11-00332.1

McPhaden MJ (1999) Genesis and evolution of the 1997–98 El Niño. Science 283(5405):950–954. https://doi.org/10.1126/science.283.5404.950%JScience

McPhaden MJ, Freitag HP, Hayes SP, Taft BA, Chen Z, Wyrtki K (1988) The response of the equatorial Pacific Ocean to a westerly wind burst in May 1986. J Geophys Res Oceans 93(C9):10589–10603. https://doi.org/10.1029/JC093iC09p10589

Neelin JD (1991) The slow sea surface temperature mode and the fast-wave limit: analytic theory for tropical interannual oscillations and experiments in a hybrid coupled model. J Atmos Sci 48:584–606. https://doi.org/10.1175/1520-0469(1991)048%3c0584:TSSSTM%3e2.0.CO;2

Park J-H, Kug J-S, An S-I, Li T (2019) Role of the Western Hemisphere Warm Pool in climate variability over the western North Pacific. Clim Dyn 53:2743–2755. https://doi.org/10.1007/s00382-019-04652-0

Philander SGH, Yamagata T, Pacanowski RC, Philander SGH, Yamagata T, Pacanowski RC (1984) Unstable air-sea interactions in the tropics. J Atmos Sci 41:604–613. https://doi.org/10.1175/1520-0469(1984)041%3c0604:UASIIT%3e2.0.CO;2

Picaut J, Masia F, du Penhoat Y (1997) An Advective-reflective conceptual model for the oscillatory nature of the ENSO. Science 277(5326):663–666. https://doi.org/10.1126/science.277.5326.663%JScience

Puy M, Vialard J, Lengaigne M, Guilyardi E (2016) Modulation of equatorial Pacific westerly/easterly wind events by the Madden–Julian oscillation and convectively-coupled Rossby waves. Clim Dyn 46:2155–2178. https://doi.org/10.1007/s00382-015-2695-x

Rong X, Zhang R, Li T, Su J (2011) Upscale feedback of high-frequency winds to ENSO. Quart J R Meteorol Soc 137:894–907

Seiki A, Takayabu YN (2007a) Westerly wind bursts and their relationship with intraseasonal variations and ENSO. Part I: Stat Month Weather Rev 135(10):3325–3345. https://doi.org/10.1175/mwr3477.1

Seiki A, Takayabu YN (2007b) Westerly wind bursts and their relationship with intraseasonal variations and ENSO. Part II: energetics over the Western and Central Pacific. Mon Weather Rev 135:3346–3361. https://doi.org/10.1175/mwr3503.1

Sikka DR, Gadgil S, Sikka DR, Gadgil S (1980) On the maximum cloud zone and the ITCZ over Indian, longitudes during the southwest monsoon. Mon Weather Rev 108(11):1840–1853. https://doi.org/10.1175/1520-0493(1980)108%3c1840:OTMCZA%3e2.0.CO;2

Smith TM et al (2008) Improvements to NOAA's historical merged land-ocean surface temperature analysis (1880–2006). J Clim 21:2283–2296. https://doi.org/10.1175/2007JCLI2100.1

Su JZ, Tao L, Renhe Z, Dake C (2018) Monitoring the pendulum between El Niño and La Niña events. Environ Res Lett 13:074001

Sui C-H, Lau K (1992) Multiscale phenomena in the tropical atmosphere over the Western Pacific. Mon Weather Rev 120(3):407–430. https://doi.org/10.1175/1520-0493(1992)120%3c0407:MPITTA%3e2.0.CO;2

Sui C-H, Li X, Lau K, Adamec D (1997) Multiscale air-sea interactions during TOGA COARE. Mon Weather Rev 125(4):448–462. https://doi.org/10.1175/1520-0493(1997)125%3c0448:MASIDT%3e2.0.CO;2

Sui C-H, Lau K, Chou S-H, Wang Z (1999) Tropical intraseasonal air-sea exchanges during the 1997 pacific warming. In: The 23rd Conference onHurricanes and Tropical Meteorology. https://ams.confex.com/ams/older/99annual/abstracts/1545.htm

Trenberth KE, Branstator GW, Karoly D, Kumar A, Lau N-C, Ropelewski C (1998) Progress during TOGA in understanding and modeling global teleconnections associated with tropical sea surface temperatures. J Geophys Res Oceans 103:14291–14324. https://doi.org/10.1029/97JC01444

Vecchi GA (2006) The termination of the 1997–98 El Niño. Part II: mechanisms of atmospheric change. J Clim 19(12):2647–2664. https://doi.org/10.1175/jcli3780

Waliser D et al (2009) MJO simulation diagnostics. J Clim 22:3006–3030. https://doi.org/10.1175/2008JCLI2731.1

Wang B, Rui H (1990) Synoptic climatology of transient tropical intraseasonal convection anomalies: 1975?1985. Meteorol Atmos Phys 44:43–61. https://doi.org/10.1007/BF01026810

Wang B, Xie X, Wang B, Xie X (1996) Low-frequency equatorial waves in vertically sheared zonal flow. Part I: stable waves. J Atmos Sci 53:449–467. https://doi.org/10.1175/1520-0469(1996)053%3c0449:LFEWIV%3e2.0.CO;2

Wang B, Zhang Q, Wang B, Zhang Q (2002) Pacific-East Asian teleconnection. Part II: how the Philippine sea anomalous anticyclone is established during El Niño development. J Clim 15:3252–3265. https://doi.org/10.1175/1520-0442(2002)015%3c3252:PEATPI%3e2.0.CO;2

Wang B, Wu R, Li T (2003) Atmosphere-warm ocean interaction and its impacts on Asian-Australian monsoon variation. J Clim. https://doi.org/10.1175/1520-0442(2003)16%3c1195:AOIAII%3e2.0.CO;2

Wang L, Li T, Zhou T (2015) Effect of high-frequency wind on intraseasonal SST variabilities over the mid-latitude North Pacific region during boreal summer. Clim Dyn 45:2607–2617. https://doi.org/10.1007/s00382-015-2496-2

Wang L, Li T, Chen L, Behera SK, Nasuno T (2018) Modulation of the MJO intensity over the equatorial western Pacific by two types of El Niño. Clim Dyn 51:687–700. https://doi.org/10.1007/s00382-017-3949-6

Wang L, Li T, Chen L (2019) Modulation of the Madden–Julian oscillation on the energetics of wintertime synoptic-scale disturbances. Clim Dyn 52:4861–4871. https://doi.org/10.1007/s00382-018-4447-1

Weng H, Ashok K, Behera SK, Rao SA, Yamagata T (2007) Impacts of recent El Niño Modoki on dry/wet conditions in the Pacific rim during boreal summer. Clim Dyn 29:113–129. https://doi.org/10.1007/s00382-007-0234-0

Wheeler M, Kiladis GN (1999) Convectively coupled equatorial waves: analysis of clouds and temperature in the wavenumber-frequency domain. J Atmos Sci 56:374–399. https://doi.org/10.1175/1520-0469(1999)056%3c0374:CCEWAO%3e2.0.CO;2

Wu B, Zhou T, Li T (2017a) Atmospheric dynamic and thermodynamic processes driving the western north pacific anomalous anticyclone during El Niño. Part I: maintenance mechanisms. J Clim 30:9621–9635. https://doi.org/10.1175/jcli-d-16-0489.1

Wu B, Zhou T, Li T (2017b) Atmospheric dynamic and thermodynamic processes driving the western north pacific anomalous anticyclone during El Niño. Part II: formation processes. J Clim 30:9637–9650. https://doi.org/10.1175/jcli-d-16-0495.1

Yu J-Y, Kim ST (2013) Identifying the types of major El Niño events since 1870. Int J Climatol 33:2105–2112. https://doi.org/10.1002/joc.3575

Yu L, Weller RA, Liu WT (2003) Case analysis of a role of ENSO in regulating the generation of westerly wind bursts in the Western Equatorial Pacific. J Geophys Res 108:3128. https://doi.org/10.1029/2002JC001498

Zhang C, Gottschalck J (2002) SST anomalies of ENSO and the Madden–Julian oscillation in the equatorial Pacific. J Clim 15:2429–2445. https://doi.org/10.1175/1520-0442(2002)015%3c2429:SAOEAT%3e2.0.CO;2